

FULL-DATA RESULTS OF HUBBLE FRONTIER FIELDS: UV LUMINOSITY FUNCTIONS AT $Z \sim 6 - 10$ AND A CONSISTENT PICTURE OF COSMIC REIONIZATION

MASAFUMI ISHIGAKI^{1,2}, RYOTA KAWAMATA³, MASAMI OUCHI^{1,4}, MASAMUNE OGURI^{2,4,5}, KAZUHIRO SHIMASAKU^{3,5},
 AND YOSHIAKI ONO¹

Accepted for publication in ApJ

ABSTRACT

We present UV luminosity functions of dropout galaxies at $z \sim 6 - 10$ with the complete Hubble Frontier Fields data. We obtain a catalog of ~ 450 dropout-galaxy candidates (350, 66, and 40 at $z \sim 6 - 7$, 8, and 9, respectively), whose UV absolute magnitudes reach ~ -14 mag, ~ 2 mag deeper than the Hubble Ultra Deep Field detection limits. We carefully evaluate number densities of the dropout galaxies by Monte-Carlo simulations, including all lensing effects such as magnification, distortion, and multiplication of images as well as detection completeness and contamination effects in a self-consistent manner. We find that UV luminosity functions at $z \sim 6 - 8$ have steep faint-end slopes, $\alpha \sim -2$, and likely steeper slopes, $\alpha \lesssim -2$ at $z \sim 9 - 10$. We also find that the evolution of UV luminosity densities shows a non-accelerated decline beyond $z \sim 8$ in the case of $M_{\text{trunc}} = -15$, while an accelerated in the case of $M_{\text{trunc}} = -17$. We examine whether our results are consistent with the Thomson scattering optical depth from the Planck satellite and the ionized hydrogen fraction Q_{HII} at $z \lesssim 7$ based on the standard analytic reionization model. We find that there exist reionization scenarios that consistently explain all the observational measurements with the allowed parameters of $f_{\text{esc}} = 0.17^{+0.07}_{-0.03}$ and $M_{\text{trunc}} > -14.0$ for $\log \xi_{\text{ion}} / [\text{erg}^{-1} \text{Hz}] = 25.34$, where f_{esc} is the escape fraction, M_{trunc} is the faint limit of the UV luminosity function, and ξ_{ion} is the conversion factor of the UV luminosity to the ionizing photon emission rate. The length of the reionization period is estimated to be $\Delta z = 3.9^{+2.0}_{-1.6}$ (for $0.1 < Q_{\text{HII}} < 0.99$), consistent with the recent estimate from Planck.

Keywords: galaxies: formation – galaxies: evolution – galaxies: high-redshift

1. INTRODUCTION

Understanding the sources of cosmic reionization is one of the goals of modern astronomy. Observational studies show that the reionization occurred at $z \gtrsim 6$ (Fan et al. 2006; Pentericci et al. 2011, 2014; Ono et al. 2012; Totani et al. 2006, 2014; Kashikawa et al. 2011; Ouchi et al. 2010; Konno et al. 2014; Treu et al. 2013). Major sources of the cosmic reionization are thought to be star-forming galaxies. Recent studies indicate that UV luminosity functions of the star-forming galaxies have steep faint-end slopes at $z \gtrsim 6$ (Bouwens et al. 2015; Schenker et al. 2013; McLure et al. 2013), which suggests that the ionizing photons are mainly supplied by faint galaxies. However, high- z galaxy observations, such as Hubble Ultra Deep Field, can reach the limiting absolute magnitudes down to $\lesssim -16$ mag at $z \gtrsim 6$. The abundance of galaxies is not well known at the magnitude fainter than ~ -16 where contributions to ionizing photon budget may be dominated. Moreover, there exist large uncertainties of various parameters to estimate an ionizing photon emission

ishigaki@icrr.u-tokyo.ac.jp

¹ Institute for Cosmic Ray Research, The University of Tokyo, 5-1-5 Kashiwanoha, Kashiwa, Chiba 277-8582, Japan

² Department of Physics, Graduate School of Science, The University of Tokyo, 7-3-1 Hongo, Bunkyo-ku, Tokyo 113-0033, Japan

³ Department of Astronomy, Graduate School of Science, The University of Tokyo, 7-3-1 Hongo, Bunkyo-ku, Tokyo 113-0033, Japan

⁴ Kavli Institute for the Physics and Mathematics of the Universe (Kavli IPMU, WPI), The University of Tokyo, 5-1-5 Kashiwanoha, Kashiwa, Chiba 277-8583, Japan

⁵ Research Center for the Early Universe, The University of Tokyo, 7-3-1 Hongo, Bunkyo-ku, Tokyo 113-0033, Japan

rate from the galaxy abundance obtained by observations. One of the important parameters is the numerical factor ξ_{ion} that converts a UV luminosity density to the ionizing photon emission rate of a star-forming galaxy. Bouwens et al. (2016a) estimated that $\log \xi_{\text{ion}} / [\text{erg}^{-1} \text{Hz}]$ has a mean value of 25.34 ± 0.02 , albeit at $z \sim 4 - 5$, the post-reionization epoch. (see also Nakajima et al. (2016) for the recent studies of ξ_{ion}). Another important parameter is the escape fraction of ionizing photons f_{esc} , which is the fraction of the number of escaping ionizing photons to that of ionizing photons produced in a galaxy. Steidel et al. (2001) estimated that the average value of f_{esc} is ~ 0.1 at $z \sim 3$ (see also Shapley et al. 2006; Iwata et al. 2009; Nestor et al. 2011; Japelj et al. 2017). Ono et al. (2010) investigated the stellar populations of Ly α emitters at $z \sim 6$, and obtained weak upper limits of $f_{\text{esc}} \sim 0.6$ at $z = 5.7$ and $f_{\text{esc}} \sim 0.9$ at $z = 6.6$, based on the constraints on the nebular emission line fluxes. Although many constraints are given by these studies, reasonable constraints on ξ_{ion} and f_{esc} at the epoch of reionization have not been obtained so far.

Gravitational lensing is an effective tool for studying high-redshift galaxies. Cluster Lensing And Supernova survey with Hubble (CLASH; Postman et al. 2012) has discovered many candidates of faint galaxies at $z \gtrsim 6$ strongly lensed by galaxy clusters. In October 2013, Hubble Frontier Fields (HFF; PI: Lotz) program has started observing six massive clusters: Abell 2744, MACSJ0416, MACSJ0717, MACSJ1149, AbellS1063, and Abell370 (Lotz et al. 2017). The HFF program achieves the limiting magnitudes ~ 29 AB mag at the 5σ level, which are ~ 1 mag deeper than those of CLASH.

Many groups study the properties of high-redshift galaxies using a part of the HFF data (Atek et al. 2015a,b; Zheng et al. 2014; Coe et al. 2015; Oesch et al. 2015; Ishigaki et al. 2015, 2016; Kawamata et al. 2015, 2016; Livermore et al. 2017; Bouwens et al. 2017a,b; McLeod et al. 2015, 2016). In September 2016, the observations for all of the six HFF clusters are completed. Here we exploit the full six cluster HFF data to investigate the galaxies at the reionization epoch.

In this paper, we first present details of the HFF data in Section 2. In Section 3, we select high-redshift galaxies with the dropout selection technique. We obtain UV luminosity functions in Section 4, and discuss the properties of the faint galaxies in Section 5. Finally, we summarize our results in Section 6. Throughout this paper, we use a cosmology with $\Omega_m = 0.3$, $\Omega_\Lambda = 0.7$, $\Omega_b = 0.04$, and $H_0 = 70 \text{ km s}^{-1} \text{ Mpc}^{-1}$.

2. DATA

For determination of UV luminosity functions, we use the complete samples of the HFF fields; Abell 2744, MACSJ0416, MACSJ0717, MACSJ1149, AbellS1063, and Abell370. Cluster and parallel fields of the six massive clusters have been observed with Advanced Camera for Surveys (ACS) and Wide Field Camera 3 (WFC3) of Hubble Space Telescope (HST) through 2013 October to 2016 September. The total survey area covers ~ 56 arcmin 2 . Drizzled and weight images are produced and released by the Space Telescope Science Institute (STScI) at the HFF Web site.⁶ The images consist of three ACS bands and four WFC3-IR bands; F435W (B_{435}), F606W (V_{606}), F814W (i_{814}), F105W (Y_{105}), F125W (J_{125}), F140W (JH_{140}), and F160W (H_{160}).

First, we homogenize the Point Spread Function (PSF) of the WFC3 images. The PSF FWHM of homogenized images is ~ 0.18 arcsec. We then measure the limiting magnitudes. We divide each image into 4×4 grid cells and define the limiting magnitude in each cell. This is because limiting magnitudes are not homogeneous due to the intra cluster light. The 5σ limiting magnitudes in the H_{160} band images are $\sim 28.5 - 29$ mag in a $0''.35$ -diameter circular aperture. Details of the PSF homogenization procedure and the limiting magnitude measurements are described in Kawamata et al. (2016) (see also Ishigaki et al. 2015). A summary of the observational properties is provided in Tables 1 and 2.

3. SAMPLES

In this study, we select i -dropout ($z \sim 6 - 7$), Y -dropout ($z \sim 8$), YJ -dropout ($z \sim 9$), and J -dropout ($z \sim 10$) galaxy candidates. A detailed description of the dropout selections is given by Kawamata et al. (2016). In this section, we give a brief description about dropout selections. First, we create detection images using SWARP (Bertin et al. 2002). The dection images are combination of J_{125} , JH_{140} , and H_{160} bands for the i - and Y -dropout selections, JH_{140} and H_{160} bands for the YJ -dropout selection, and H_{160} band for the J -dropout selection, respectively. We run SExtractor (version 2.8.6; Bertin & Arnouts 1996) in dual-image mode using the detection images, and create photometric catalogs. The colors of galaxies are measured with `MAG_APER` m_{AP} . The total

magnitudes of galaxies m_{tot} are defined with the equation $m_{tot} = m_{AP} - 0.82$, where the offset 0.82 corresponds to the aperture correction and was derived in Ishigaki et al. (2015). Selection criteria of i -dropout galaxies are

$$i_{814} - Y_{105} > 0.8, \quad (1)$$

$$Y_{105} - J_{125} < 0.8, \quad (2)$$

$$i_{814} - Y_{105} > 2(Y_{105} - J_{125}) + 0.6, \quad (3)$$

which are used in Atek et al. (2015b). We require the detection significance levels beyond 5σ level in the Y_{105} band and J_{125} band. We exclude the objects that are detected at the 2σ level in both the B_{435} and V_{606} bands or in the $B_{435} + V_{606}$ stacked images.

For Y -dropouts, we adopt the selection criteria given by Atek et al. (2014):

$$Y_{105} - J_{125} > 0.5, \quad (4)$$

$$J_{125} - JH_{140} < 0.5, \quad (5)$$

$$Y_{105} - J_{125} > 1.6(J_{125} - JH_{140}) + 0.4. \quad (6)$$

Similarly, we apply the source detection thresholds of the $> 5\sigma$ significance levels in the J_{125} , JH_{140} , and H_{160} bands. We remove the objects that are detected at the 2σ level in at least one of the B_{435} , V_{606} , or i_{814} bands.

For YJ -dropouts, we use criteria presented in Oesch et al. (2013) and Ishigaki et al. (2015):

$$(Y_{105} + J_{125})/2 - JH_{140} > 0.75, \quad (7)$$

$$(Y_{105} + J_{125})/2 - JH_{140} > 0.8(JH_{140} - H_{160}) + 0.75, \quad (8)$$

$$J_{125} - H_{160} < 1.15, \quad (9)$$

$$JH_{140} - H_{160} < 0.6. \quad (10)$$

We require the detection significance levels beyond 3σ level in both the JH_{140} and H_{160} bands and 3.5σ level in one of the JH_{140} or H_{160} bands. Again, we remove the objects that are detected at the 2σ level in the B_{435} , V_{606} , or i_{814} bands.

For J -dropouts, we apply the criteria used in Oesch et al. (2015):

$$J_{125} - H_{160} > 1.2, \quad (11)$$

$$S/N(B_{435} \text{ to } Y_{105}) < 2. \quad (12)$$

We also require $\chi_{opt+Y}^2 < 2.5$, where χ_{opt+Y}^2 is defined by $\chi_{opt+Y}^2 \equiv \sum_n \text{SGN}(f_n)S/N(n)^2$. f_n is the n th band flux in B_{435} , V_{606} , i_{814} , and Y_{105} . $\text{SGN}(f_n)$ is a sign function. S/N s in the JH_{140} and H_{160} bands are required to be $> 3.5\sigma$ in both bands and $> 5\sigma$ in one of the two bands. Finally, spurious sources are removed from the dropout galaxy candidates by visual inspection.

In this study, we find no J -dropout candidates in the all cluster and parallel fields. Our dropout samples consist of 350 i -dropouts, 66 Y -dropouts, and 40 YJ -dropouts in total. The number of the dropout candidates in each field is listed in Table 1. We list these dropout candidates in Tables 4, 5, and 6. The values of magnitudes are slightly different from those in Kawamata et al. (2016) because Kawamata et al. (2016) used an older version of SExtractor.

⁶ <http://www.stsci.edu/hst/campaigns/frontier-fields/>

4. UV LUMINOSITY FUNCTIONS

Table 1
Observational properties and the numbers of high- z galaxy candidates of the HFF Data

Field	Depth (H_{160}) ^a (5 σ limit mag)	Area ^b (arcmin 2)	Number of Galaxies			
			$z \sim 6 - 7$	$z \sim 8$	$z \sim 9$	$z \sim 10$
Abell2744 Cluster	28.88	4.75 (1.52 ^c)	22	10	3	0
Abell2744 Parallel	29.11	4.32	30	4	4	0
MACS0416 Cluster	28.84	4.73 (2.00 ^c)	25	5	3	0
MACS0416 Parallel	29.30	4.78	23	9	6	0
MACS0717 Cluster	28.56	4.58 (0.75 ^c)	22	0	0	0
MACS0717 Parallel	28.88	4.25	41	6	3	0
MACS1149 Cluster	28.87	4.66 (1.32 ^c)	41	2	4	0
MACS1149 Parallel	29.04	4.72	37	10	3	0
AbellS1063 Cluster	28.85	4.25 (0.98 ^c)	23	4	2	0
AbellS1063 Parallel	29.12	4.36	39	6	3	0
Abell370 Cluster	28.65	4.14 (0.73 ^c)	7	6	2	0
Abell370 Parallel	29.14	4.31	40	3	7	0
Total			350	66	40	0

^a The depths are defined with a 0. $'$ 35-diameter aperture.

^b The area of each image is reduced by the masking near the bright stars.

^c The survey area in the source plane at $z = 7$.

Table 2
 5σ limiting magnitudes

Field	B_{435}	V_{606}	i_{814}	Y_{105}	J_{125}	JH_{140}	H_{160}
Abell2744 Cluster	28.72	28.83	28.94	29.20	28.87	28.92	28.88
Abell2744 Parallel	28.84	29.20	29.03	29.39	29.00	29.03	29.11
MACS0416 Cluster	28.74	29.08	28.96	29.11	28.85	28.87	28.84
MACS0416 Parallel	28.65	28.92	29.01	29.45	29.22	29.26	29.30
MACS0717 Cluster	28.70	28.74	28.76	28.91	28.61	28.70	28.56
MACS0717 Parallel	28.96	29.00	29.01	29.16	28.94	28.95	28.88
MACS1149 Cluster	28.57	28.89	28.94	29.17	28.81	28.73	28.87
MACS1149 Parallel	28.50	28.83	28.90	29.35	28.98	29.06	29.04
AbellS1063 Cluster	28.69	28.86	28.90	29.19	28.87	28.98	28.85
AbellS1063 Parallel	28.87	29.66	29.09	29.43	29.06	29.19	29.12
Abell370 Cluster	28.64	28.78	28.86	29.00	28.69	28.74	28.65
Abell370 Parallel	28.65	28.90	29.07	29.45	29.00	29.01	29.14

In this section, we calculate UV luminosity functions at $z \sim 6 - 7$, 8, 9, and 10. UV luminosity functions are represented by the Schechter function with three parameters; ϕ_* , M_* , and α :

$$\Phi(M_{\text{UV}}, \phi_*, M_*, \alpha) dM_{\text{UV}} = 0.4\phi_* \ln(10) \times \exp \left[10^{-0.4(M_{\text{UV}} - M_*)} \right] 10^{-0.4(\alpha+1)(M_{\text{UV}} - M_*)} dM_{\text{UV}}. \quad (13)$$

We derive the luminosity functions basically in the same manner as that described in Section 5 of Ishigaki et al. (2015), that adopt the luminosity function fitting on the image plane. We refer to the method as the image plane method in the remainder of this paper. The image plane method deals with not only the lensing magnification effects, but also the distortion and multiplication of lensed images in a self-consistent way. Oesch et al. (2015) showed that the detection completeness of galaxies strongly depends on the galaxy size and the image distortion, especially at areas with high magnifications. It is critical to properly evaluate the lensing effects and the properties of high-redshift galaxies to derive the luminosity functions, as done in this paper. In this study, we define M_{UV} as the magnitude in the rest-frame wavelength of 1500Å. This wavelength roughly corresponds to J_{125} , JH_{140} , H_{160} , and H_{160} bands at $z \sim 6 - 7$, 8, 9, and 10, respectively.

In section 4.1, we create mock catalogs of high-redshift

galaxies and obtain number densities on the image plane. In section 4.2, we compare number densities of the mock catalogs with those of the observation, and determine the best fit Schechter parameters.

4.1. Creation of Mock Catalogs

We create mock catalogs of simulated high-redshift galaxies at $z \sim 5.0 - 12$. The number densities of the galaxies follow the Schechter functions. The half-light radius of the galaxies are ~ 0.45 , ~ 0.22 , and ~ 0.11 kpc for galaxies with magnitudes of $M_{\text{UV}} < -20$, $-20 < M_{\text{UV}} < -16$, and $M_{\text{UV}} > -16$, respectively. This assumption is consistent with the size-luminosity relations adopted in previous studies. The Sérsic index is assumed to be 1. The ellipticities are randomly chosen from the range of 0.0–0.9, because high-redshift galaxy studies show roughly uniform distributions of the ellipticities (e.g. Ravindranath et al. 2006). The UV spectral slope β is assumed to be $\beta = -2$, which is consistent with the result of Bouwens et al. (2014). The UV spectra are attenuated with the IGM absorption model of Madau et al. (1996). The mock galaxies are distributed in random positions of the source plane. We create images of the mock galaxies with `writeimage` function in the lens model software `GLAFIC` (Oguri 2010). The `writeimage` function calculates the gravitational lensing effects including magnification, distortion, and multiplication, for an object and produce the image(s) in the image plane.

Here we use the mass models of the six clusters described in Kawamata et al. (2016) and Kawamata et al. (2017). Three out of the six models are released in the HFF Web site⁷ as version 3 for Abell 2744, MACS0717, and MACS1149. We use an updated version of the mass model for MACS0416 (Kawamata et al. 2017). In the parallel fields, we use `writeimage_ori` function, which creates unlensed images. We add the simulated images in the real HFF data. Then we detect the mock galaxies with SExtractor and select dropouts in the mock catalogs with the color criteria same as the observations described in Section 3. We obtain number densities of dropouts in the mock catalogs.

Low-redshift galaxies are potentially contaminate the dropout catalogs of the observational data. We estimate the contamination rate by the following procedure. First, we create the catalogs of bright ($22 < H_{160} < 25$) objects in the HFF images. In this magnitude range, all objects do not meet the color criteria of the dropouts, which are probably low-redshift interlopers. Then we create interloper catalogs of faint objects ($25 < H_{160} < 29$). We fit the number densities of the bright interlopers with a power-law function, and match the number densities of the faint interlopers to those extrapolated from the bright magnitudes. We assume that the physical properties of faint interlopers such as the color and size are the same as those of the bright objects. We create images of artificial objects from these catalogs with the `mkobjects` package of IRAF, and randomly place them on the HFF images. We detect the artificial objects with SExtractor, and select the artificial objects that meet the dropout selection criteria. We regard these selected objects as contaminants. We thus obtain the contamination rate of dropouts as a function of magnitude. The contamination rate is $\sim 9\%$ ($\sim 32\%$) in the magnitude range of $M_{UV} < 27.25$ ($M_{UV} > 27.25$) on average. We add the number densities of the contaminants to the total number densities of the dropouts in the mock catalogs.

4.2. Luminosity Function Fitting

We compare the observed number densities of dropouts with the number density obtained in the simulations, which is described in the Section 4.1. We obtain the best-fit luminosity function by fitting these number densities with a maximum likelihood method. We calculate the likelihood with the following equation, assuming the Poisson errors:

$$\mathcal{L} \propto \prod_{\text{field}} \prod_i n_{\text{sim},i}^{n_{\text{obs},i}} e^{-n_{\text{sim},i}}, \quad (14)$$

where $n_{\text{sim},i}$ is the simulated number counts in an i th magnitude bin, and $n_{\text{obs},i}$ is the observed number counts in the HFF in the magnitude bin. We treat the three Schechter parameters, ϕ_* , M_* , and α , as free parameters in the fitting of luminosity functions at $z \sim 6 - 7$ and 8. The number counts at $z \sim 9$ and $z \sim 10$ have too poor statisticis to constrain the three Schechter parameters. Therefore, we also provide results where we treat ϕ_* as the only free parameter at $z \sim 9$ and 10, and fix M_* and α to the values at $z \sim 8$, -20.35 and -1.96 , respectively. In order to improve the statistics, we simultaneously fit our number counts data and UV luminosity

function data points from previous studies. We use recent results of blank field surveys; Bouwens et al. (2015); Bowler et al. (2014); Ouchi et al. (2009); Bradley et al. (2012); Oesch et al. (2013); Calvi et al. (2016). Although Schmidt et al. (2014) presented an updated result of the BoRG survey (Bradley et al. 2012), we do not incorporate their result because they do not provide number densities at individual magnitudes. We iterate the luminosity function fitting with various Schechter parameter sets, and obtain the best-fit parameters.

One of the advantages of the image plane method is that the result is not affected by uncertainties of magnification factors of dropout candidates. If a galaxy has magnification factor larger than ~ 100 , the 1σ error of the magnification is as large as itself (Tables 10 to 12 in Kawamata et al. 2016). Luminosity function fitting on the source plane has large uncertainty in the faint end, because the galaxy samples in the faint magnitude bins consists of galaxies with high magnification factors. The disadvantage of the image plane method is that there is a degeneracy between number densities of intrinsically bright and faint galaxies with the same apparent magnitude. The constraints on the faint end of luminosity functions are weaker than those with fitting on the source plane. In order to strengthen the constraints on the faint end, we divide the dropout samples into subsamples with magnification factor binning of $\mu < 2$, $2 < \mu < 6$, $6 < \mu < 18$, and $\mu > 18$ at $z \sim 6 - 7$. We use the surface number density in each magnitude bin and in each magnification factor bin for fitting. Note that the number densities divided with magnification factor bins depend on mass models, although the uncertainty is not larger than the one in fitting on the source plane. We estimate the uncertainty of mass models in the end of this section. At $z \gtrsim 8$, we do not divide the samples, because the number of $z \gtrsim 8$ galaxy candidates is not large enough for making subsamples.

The best-fit parameters are shown in Table 3. We find that the uncertainties in M_* and ϕ_* are considerably large due to a degeneracy between the two parameters when all parameters are variable. Plotted in Figure 1 is the faint-end slope α as a function of redshift. Our results indicate that the best-fit values of α are about -2 at $z \sim 6 - 7$ to 10, which are steeper than those at lower redshift (e.g. $\alpha \sim -1.6$ at $z \sim 4$ in Bouwens et al. 2015). We show the fitting results at $z \sim 6 - 7$, 8, 9, and 10 in Figures 2, 3, 4, and 5, respectively. The top and bottom panel present the observed number densities and the best-fit luminosity functions in the image plane and the source plane, respectively. We also plot the results of previous blank-field surveys (Bouwens et al. 2015; Bowler et al. 2014; Ouchi et al. 2009; Schenker et al. 2013; Bradley et al. 2012; Finkelstein et al. 2015; McLure et al. 2013; Oesch et al. 2013; Calvi et al. 2016) and recent HFF results in other studies (Laporte et al. 2016; Atek et al. 2015a; McLeod et al. 2016). The best-fit parameters are consistent with those in previous studies. In the top panel of Figure 2, there may be an excess in the observed surface number density at $J_{125} = 28.5$. The reason for this excess is not clear, although using a size-luminosity relation which gives smaller sizes at faint magnitudes may reduce this excess. At $z \sim 8$, the observed number densities at the bright end are slightly larger than the number densities in the simulation. It is

⁷ <https://archive.stsci.edu/prepds/frontier/lensmodels/>

probably due to the existence of an overdense region of $z \sim 8$ dropouts in the Abell 2744 cluster field. We discussed the properties of the overdensity in Ishigaki et al. (2016) (see also Atek et al. 2015b and Zheng et al. 2014). At $z \sim 10$, although we detect no galaxies, we can place a constraint on the luminosity function from the non-detection. Based on the best-fit parameters where only ϕ_* is variable, ~ 1.4 galaxies are expected to be detected in the HFF fields. The middle panels of Figures 2–5 show histograms of the number of the dropouts. It is seen that our samples push the magnitude limits of the luminosity functions significantly by up to ~ 3 magnitude.

Bouwens et al. (2017b) claim that the accuracy of UV luminosity functions is limited due to the uncertainty of mass models. In order to estimate the uncertainty of mass models with the method we use for the luminosity function at $z \sim 6 - 7$, we check the magnification factors of the dropout candidates with five different mass models from Bradac (v2 for Abell 2744, v3 for MACS0416, and v1 for MACS0717, MACS1149, AbellS1063, and Abell370; Wang et al. 2015, Hoag et al. 2016, see also Bradač et al. 2009), CATS (v3.1 for Abell 2744, v3.1 for MACS0416, v1 for MACS0717, MACS1149, AbellS1063, and Abell370; Jauzac et al. 2015), Sharon (v3 for Abell 2744 and MACS0416, v2 for MACS0717, v2.1 for MACS1149, v1 for Abell370 and Abells1063; Johnson et al. 2014), Williams (v3 for Abell 2744, v3.1 for MACS0416, v1 for MACS0717, MACS1149, AbellS1063, and Abell370), and Zitrin (LTM v1 for all the six clusters; Zitrin et al. 2009, Zitrin et al. 2013). We obtain the UV luminosity functions at $z \sim 6 - 7$ with these five different mass models. Figure 7 shows the best-fit Schechter parameters and the 68% and 95% confidence levels. We confirm that the difference of the best-fit parameters are $\Delta\phi_* \sim 0.2$, $\Delta M_* \sim 0.2$, and $\Delta\alpha \sim 0.1$, which are comparable to the statistical errors of these parameters (Table 3). Magnification factor of each dropout could be different from others in different mass model (see also Figure 11 of Ishigaki et al. 2015), but the values of the best-fit Schechter parameters are almost the same in all the mass models.

5. DISCUSSION

In the previous section, we derive the UV luminosity functions at $z \sim 6 - 10$ from the HFF data and the previous blank field data. In this section, we estimate the UV luminosity densities ρ_{UV} from the luminosity functions which constrain the physical properties of ionizing sources and reionization.

5.1. Evolution of the UV Luminosity Density

The value of ρ_{UV} is calculated with the following equation:

$$\rho_{\text{UV}}(z) = \int_{-\infty}^{M_{\text{trunc}}} \Phi(M) L(M) dM, \quad (15)$$

where $L(M)$ is the UV luminosity corresponding to the UV magnitude M . The value of M_{trunc} is the truncation magnitude of the UV luminosity function, i.e., there are no galaxies with the magnitudes fainter than M_{trunc} . We calculate ρ_{UV} at $z \sim 6 - 7, 8, 9$, and 10 using the best-fit Schechter functions obtained in Section 4.2. Figure 8 shows ρ_{UV} calculated from Equation (15) with $M_{\text{trunc}} =$

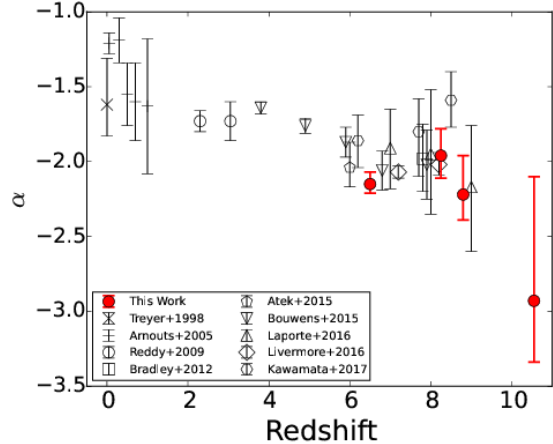


Figure 1. Redshift evolution of the faint-end slope α of the rest-frame UV luminosity function. The red circles show our results and the black symbols show the values of local UV-selected galaxies (Treyer et al. 1998), $0.2 \leq z \leq 1.2$ galaxies (Arnouts et al. 2005), $1.9 \leq z \leq 3.4$ LBGs (Reddy & Steidel 2009), $z \sim 8$ LBGs (Bradley et al. 2012), $z \sim 6$ LBGs (Atek et al. 2015a), $z \sim 4 - 8$ LBGs (Bouwens et al. 2015), $z \sim 7 - 9$ LBGs (Laporte et al. 2016), $z \sim 7 - 8$ LBGs (Livermore et al. 2017), and $z \sim 6 - 9$ LBGs (Kawamata et al. 2017).

-15.0 and $M_{\text{trunc}} = -17.0$. The right axis in Figure 8 presents cosmic star formation rate densities (SFRDs) from a given luminosity density that are estimated from ρ_{UV} based on Equation (2) of Madau et al. (1998).

For comparisons, we also show the data plots of ρ_{UV} with $M_{\text{trunc}} = -15.0$ and $M_{\text{trunc}} = -17.0$ at $z \sim 4 - 12$ that are taken from previous studies (Bouwens et al. 2015; McLeod et al. 2016; Coe et al. 2013; Ellis et al. 2013). In Figure 8, we include total ρ_{UV} at $z \sim 0 - 3$ (Steidel et al. 1999; Wyder et al. 2005; Schiminovich et al. 2005; Reddy & Steidel 2009), and cosmic SFRDs at $z \sim 1 - 4$ based on ρ_{UV} ($M_{\text{trunc}} = -15.0$) and IR luminosity densities (the sensitivity corresponding to $\simeq 30 \mu\text{Jy}$) (Dunlop et al. 2017). Our results are consistent with these previous studies at $z \sim 6 - 10$.

Our results support a non-accelerated decline of ρ_{UV} toward high redshifts in the case of $M_{\text{trunc}} = -15.0$ (see also McLeod et al. 2016). We check whether we can approximate the evolution of $\log \rho_{\text{UV}}$ from $z = 4$ to 10 as a linear function. We fit the $\log \rho_{\text{UV}}$ from this work and Bouwens et al. (2015) with linear and quadratic functions. The Akaike Information Criterion corrected for small data sets (AICc; Sugiura 1978) for the linear function is smaller by $\Delta \text{AICc} = 3.69$ than that for the quadratic function, suggesting a non-accelerated ρ_{UV} evolution.

However, we find an accelerated decline when a brighter truncation magnitude of $M_{\text{trunc}} = -17.0$ is adopted, which is closer to $M_{\text{trunc}} = -17.7$ adopted in Oesch et al. (2013), who support an accelerated decline. In Figure 8, we present fitting results to ρ_{UV} in this work and Bouwens et al. (2015) with a linear function at $z \sim 4 - 8$ and its extrapolation toward $z \sim 10$. This indicates the trends of non-accelerated and accelerated declines in the cases of $M_{\text{trunc}} = -15.0$ and -17.0 , respectively. One possible explanation for this dependence on M_{trunc} is the evolution of the faint-end slope toward steeper value at higher redshifts (see Figure 1).

Table 3
Best-fit Schechter parameters of luminosity functions

Reference	M_*	$\log \phi_* [\text{Mpc}^{-3}]$	α
$z \sim 6 - 7$			
This Work	$-20.89^{+0.17}_{-0.13}$	$-3.78^{+0.15}_{-0.15}$	$-2.15^{+0.08}_{-0.06}$
Atek et al. (2015a)	$-20.89^{+0.60}_{-0.72}$	$-3.54^{+0.48}_{-0.45}$	$-2.04^{+0.17}_{-0.13}$
Bouwens et al. (2015)	-20.87 ± 0.26	$-3.53^{+0.24}_{-0.23}$	-2.06 ± 0.13
Laporte et al. (2016)	$-20.33^{+0.37}_{-0.47}$	$-3.43^{+0.12}_{-0.15}$	$-1.91^{+0.26}_{-0.27}$
Livermore et al. (2017)	$-20.800^{+0.058}_{-0.049}$	$-3.667^{+0.044}_{-0.041}$	$-2.07^{+0.04}_{-0.04}$
Kawamata et al. (2017)	$-20.73^{+0.46}_{-0.81}$	—	$-1.86^{+0.17}_{-0.18}$
$z \sim 8$			
This Work	$-20.35^{+0.20}_{-0.30}$	$-3.60^{+0.15}_{-0.30}$	$-1.96^{+0.18}_{-0.15}$
Bradley et al. (2012)	$-20.26^{+0.29}_{-0.34}$	$-3.37^{+0.26}_{-0.29}$	$-1.98^{+0.23}_{-0.22}$
Bouwens et al. (2015)	-20.63 ± 0.36	-3.68 ± 0.32	-2.02 ± 0.23
Laporte et al. (2016)	$-20.32^{+0.49}_{-0.26}$	$-3.52^{+0.58}_{-0.44}$	$-1.95^{+0.43}_{-0.40}$
Livermore et al. (2017)	$-20.742^{+0.195}_{-0.152}$	$-3.784^{+0.145}_{-0.145}$	$-2.02^{+0.08}_{-0.07}$
Kawamata et al. (2017)	-20.73 (fixed)	—	$-1.80^{+0.22}_{-0.30}$
$z \sim 9$			
This Work	$-51.39^{+18.51}_{-44.73}$	$-19.42^{+7.73}_{-24.15}$	$-2.22^{+0.26}_{-0.17}$
This Work	-20.35 (fixed)	$-3.88^{+0.08}_{-0.12}$	-1.96 (fixed)
Oesch et al. (2013)	-18.8 ± 0.3	-2.94 (fixed)	-1.73 (fixed)
Laporte et al. (2016)	-20.45 (fixed)	$-4.15^{+0.15}_{-0.24}$	$-2.17^{+0.41}_{-0.43}$
McLeod et al. (2016)	-20.1 (fixed)	$-3.62^{+0.08}_{-0.10}$	-2.02 (fixed)
Kawamata et al. (2017)	-20.73 (fixed)	—	$-1.59^{+0.19}_{-0.18}$
$z \sim 10$			
This Work	$-59.71^{+29.90}_{-9.61}$	$-35.60^{+23.73}_{-5.93}$	$-2.93^{+0.83}_{-0.41}$
This Work	-20.35 (fixed)	$-4.60^{+0.14}_{-0.22}$	-1.96 (fixed)
Oesch et al. (2014)	-20.12 (fixed)	-4.27 ± 0.21	-2.02 (fixed)
Bouwens et al. (2015)	-20.92 (fixed)	$-5.10^{+0.18}_{-0.20}$	-2.27 (fixed)
McLeod et al. (2016)	-20.1 (fixed)	$-3.90^{+0.13}_{-0.20}$	-2.02 (fixed)

The faint-end slope steepening makes the ρ_{UV} difference (between the cases of $M_{\text{trunc}} = -15.0$ and -17.0) larger at $z \sim 10$ than at $z \sim 8$. The redshift evolution of M_* toward fainter magnitudes (see Figure 6) would also contribute to this larger increases of ρ_{UV} at higher redshifts.

On the other hand, our previous study in Ishigaki et al. (2015) has claimed that ρ_{UV} shows an accelerated decrease beyond $z \sim 8$. This can be because they adopt a brighter truncation magnitude of $M_{\text{trunc}} = -17.0$. Another possible explanation for the difference is cosmic variance. Ishigaki et al. (2015) only use the data of Abell 2744 cluster and parallel fields. In these fields, the galaxy density at $z \sim 8$ is ~ 0.1 dex higher than the average of total fields (Ishigaki et al. 2016), and the one at $z \sim 9$ is ~ 0.1 dex lower than the average.

5.2. Properties of the Ionizing Sources

In this section, we calculate the ionized hydrogen fraction Q_{HII} and the Thomson scattering optical depth τ_e , basically in the same manner as that described in Section 5 of Ishigaki et al. (2015).

The value of Q_{HII} is calculated with the following equation (e.g. Robertson et al. 2013):

$$\dot{Q}_{\text{HII}} = \frac{\dot{n}_{\text{ion}}}{\langle n_{\text{H}} \rangle} - \frac{Q_{\text{HII}}}{t_{\text{rec}}}. \quad (16)$$

In the first term of Equation (16), \dot{n}_{ion} and $\langle n_{\text{H}} \rangle$ denote the production rate of ionizing photons and the mean

hydrogen number density, respectively. \dot{n}_{ion} and $\langle n_{\text{H}} \rangle$ are defined by the following equations:

$$\begin{aligned} \dot{n}_{\text{ion}} &= \int_{-\infty}^{M_{\text{trunc}}} f_{\text{esc}}(M_{\text{UV}}) \xi_{\text{ion}}(M_{\text{UV}}) \Phi(M_{\text{UV}}) L(M_{\text{UV}}) dM_{\text{UV}} \\ &\equiv \langle f_{\text{esc}} \xi_{\text{ion}} \rangle \rho_{\text{UV}}, \end{aligned} \quad (17)$$

$$\langle n_{\text{H}} \rangle = \frac{X_{\text{P}} \Omega_{\text{b}} \rho_{\text{c}}}{m_{\text{H}}}, \quad (18)$$

where X_{P} is the primordial mass fraction of hydrogen, ρ_{c} is the critical density, and m_{H} is the mass of the hydrogen atom. f_{esc} is the fraction of the number of escaping ionizing photons to those produced in a galaxy. ξ_{ion} is the numerical factor that converts a UV luminosity density to the ionizing photon emission rate of a star-forming galaxy. Note that f_{esc} and ξ_{ion} appear in the product form in Equation (17). Here we assume that f_{esc} and ξ_{ion} do not depend on M_{UV} . We present the magnitude-averaged value of the product of f_{esc} and ξ_{ion} as $\langle f_{\text{esc}} \xi_{\text{ion}} \rangle$. In the second term of Equation (16), t_{rec} represents the averaged gas recombination time:

$$t_{\text{rec}} = \frac{1}{C_{\text{HII}} \alpha_{\text{B}}(T) (1 + Y_{\text{p}}/4X_{\text{p}}) \langle n_{\text{H}} \rangle (1+z)^3}, \quad (19)$$

where α_{B} is the case-B hydrogen recombination coefficient, T is the IGM temperature, and Y_{p} is the primordial helium mass fraction. $C_{\text{HII}} \equiv \langle n_{\text{HII}}^2 \rangle / \langle n_{\text{HII}} \rangle^2$ is a clumping factor, where n_{HII} is the local number density

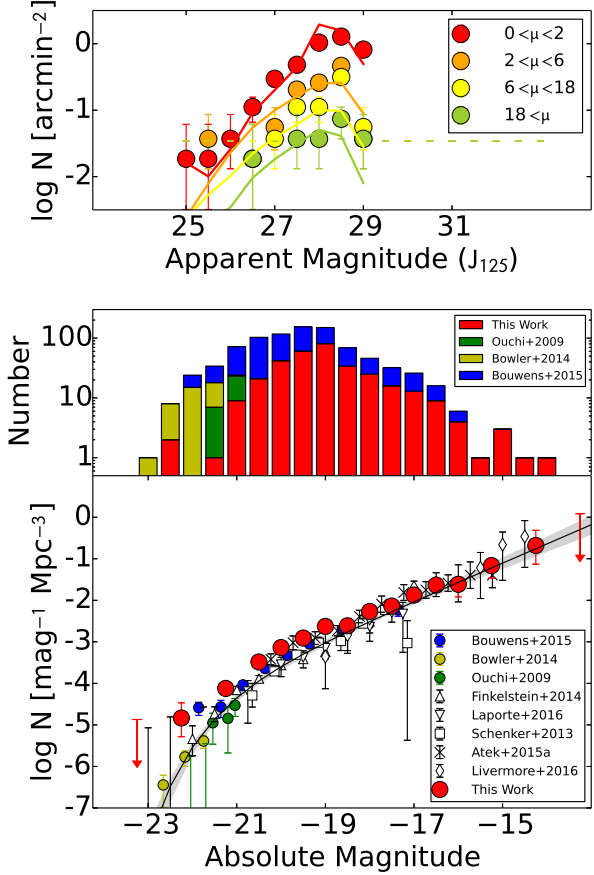


Figure 2. Surface number densities, histograms of number counts, and luminosity functions of $z \sim 6 - 7$ dropout candidates. Top panel: surface number densities of our dropout candidates in the HFF data (circles) and those derived from the best-fit Schechter function (lines). The colors of the circles and lines denote the magnification factor of $0 < \mu < 2$ (red), $2 < \mu < 6$ (orange), $6 < \mu < 18$ (yellow), and $18 < \mu$ (green). The horizontal axis shows the apparent magnitude in the J_{125} band. Middle panel: histograms of the number counts of dropouts in our study (red) and previous studies: Ouchi et al. (2009) (green), Bowler et al. (2014) (yellow), and Bouwens et al. (2015) (blue). Bottom panel: best-fit Schechter function (black line) with the 1σ error (gray region) and the luminosity functions derived by this work (red circles), Bouwens et al. (2014) (blue circles), Bowler et al. (2014) (yellow circles), Ouchi et al. (2009) (green circles), Finkelstein et al. (2015) (open up-triangles), Laporte et al. (2016) (open down-triangles), Schenker et al. (2013) (open squares), Atek et al. (2015a) (crosses), and Livermore et al. (2017) (open diamonds). The horizontal axis presents the absolute magnitude in the J_{125} band.

of ionized hydrogen. In this work, we use the following equation:

$$C_{\text{H}_{\text{II}}} = 2.9 \times \left[\frac{(1+z)}{6} \right]^{-1.1}, \quad (20)$$

which was obtained from the hydrodynamical + N -body simulations in Shull et al. (2012). The value of the clumping factor is not accurately known observationally, although many theoretical studies suggest similar values of clumping factor, $C_{\text{H}_{\text{II}}} \sim 1 - 6$, in the epoch of reionization (Sokasian et al. 2003; Iliev et al. 2006; Finlator et al. 2012).

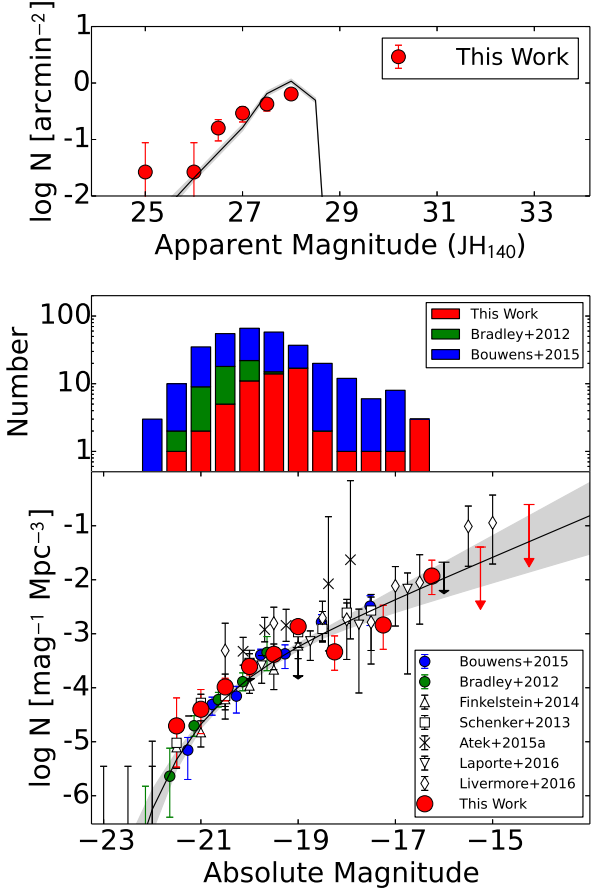


Figure 3. Same as Figure 2, but for $z \sim 8$. The horizontal axes in the top and bottom panels present the apparent and intrinsic magnitudes in the JH_{140} band, respectively. The results of Bradley et al. (2012) are shown with the green histogram (middle panel) and circles (bottom panel). In the bottom panel, we also plot the result of Livermore et al. (2017) with the open diamonds.

The value of τ_e is calculated with the following equation (Kuhlen & Faucher-Giguère 2012):

$$\tau_e(z) = \int_0^z \frac{c(1+z')^2}{H(z')} Q_{\text{HII}} \sigma_T \langle n_H \rangle \times (1 + \eta Y_p / 4X_p) dz', \quad (21)$$

where $H(z)$ is the Hubble parameter, σ_T is the Thomson scattering cross section, and c is the speed of light. We assume that helium is singly ionized (corresponding to $\eta = 1$) at $z > 4$ and doubly ionized (corresponding to $\eta = 2$) at $z \leq 4$, following Kuhlen & Faucher-Giguère (2012). Recently, Planck Collaboration et al. (2016) have obtained $\tau_e = 0.058 \pm 0.012$ from the measurement of TT power spectrum and EE polarization of CMB. The value of τ_e from Planck Collaboration et al. (2016) is smaller than the one obtained in previous observations by nine-year WMAP ($\tau_e = 0.088 \pm 0.013$, Bennett et al. 2013; Hinshaw et al. 2013) and Planck 2014 ($\tau_e = 0.092 \pm 0.013$, Planck Collaboration et al. 2014).

We assume the following two functional form of ρ_{UV} . One is the four-parameter function from Madau & Dick-

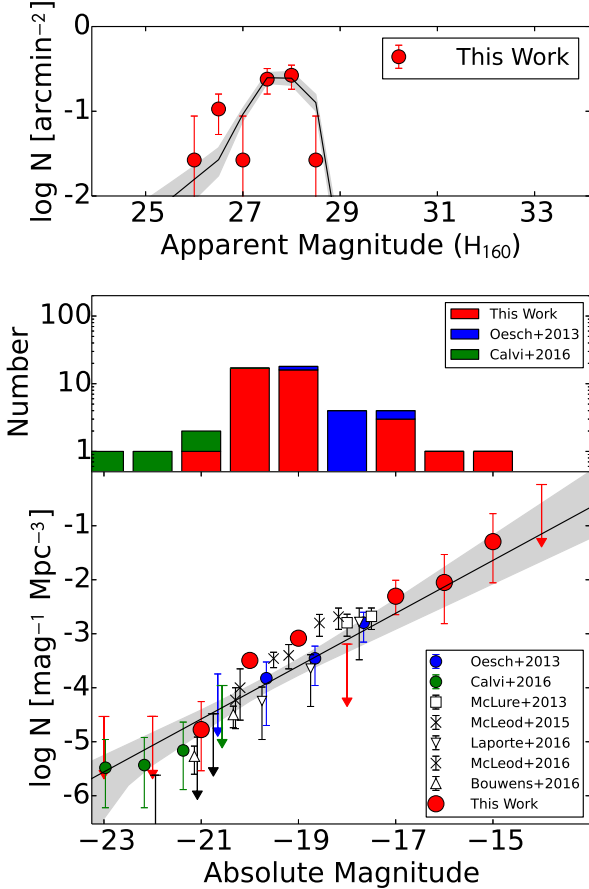


Figure 4. Same as Figure 2, but for $z \sim 9$. The horizontal axes in the top and bottom panels present the apparent and intrinsic magnitudes in the H_{160} band, respectively. The blue (green) histogram and circles denote the results of Oesch et al. (2013) (Calvi et al. 2016), respectively. In the bottom panel, we also plot the results of McLure et al. (2013) (open squares), McLeod et al. (2015, 2016) (crosses), and Bouwens et al. (2016b) (open triangles).

inson (2014) (see also Robertson et al. 2015):

$$\rho_{\text{UV}}(z) = a_p \frac{(1+z)^b}{1 + [(1+z)/c_p]^d}, \quad (22)$$

which has free parameters of a_p , b_p , c_p , and d_p . The other is a logarithmic double power law function used in Ishigaki et al. (2015):

$$\rho_{\text{UV}}(z) = \frac{2\rho_{\text{UV}}^*}{10^{a(z-z_*)} + 10^{b(z-z_*)}}, \quad (23)$$

which also has four free parameters; ρ_{UV}^* , z_* , a , and b . We perform χ^2 fitting to the observational data of ρ_{UV} , Q_{HII} , and τ_e . In each parameter space, we adopt one of the two functional forms of $\rho_{\text{UV}}(z)$ whose minimum χ^2 is smaller than the one of the other. We use the ρ_{UV} data points at $z \sim 6 - 7$, 8 , 9 , and 10 (this work) and $z \sim 4$, 5 , and 6 (Bouwens et al. 2015) that are presented in the left panel of Figure 9. Although ρ_{UV} at $z \sim 10$ scatters upward due to the large uncertainty in α , this does not significantly affect the fitting

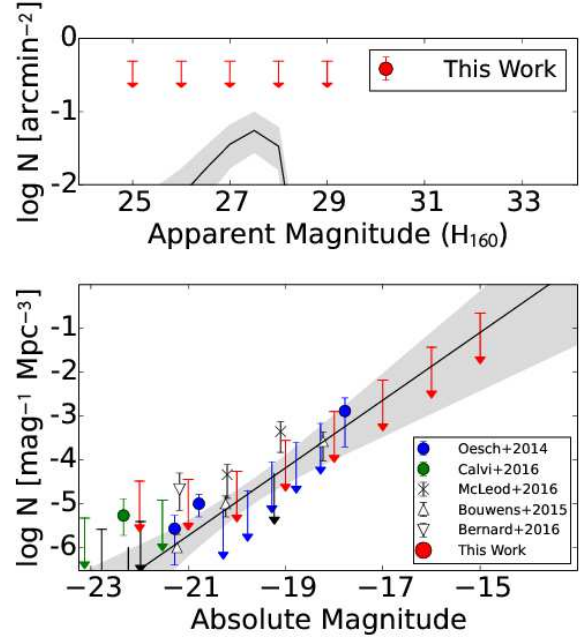


Figure 5. Same as Figure 2, but for $z \sim 10$. The horizontal axes in the top and bottom panels present the apparent and intrinsic magnitudes in the H_{160} band, respectively. The blue (green) circles denote the results of Oesch et al. (2014) (Calvi et al. 2016), respectively. In the bottom panel, we also plot the results of Bernard et al. (2016) (open down-triangles), McLeod et al. (2016) (crosses), and Bouwens et al. (2015) (open up-triangles).

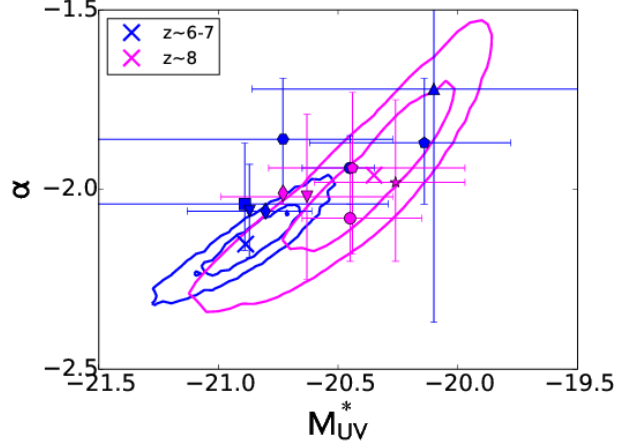


Figure 6. Contours of Schechter parameters M_* and α indicating the 68% and 95% confidence levels. In this plot, blue (magenta) symbols on lines denote $z \sim 6 - 7$ ($z \sim 8$). The values of the best-fit Schechter parameters are shown with the cross symbols. We plot the best-fit parameters from previous studies: Ishigaki et al. (2015) (circles), Atek et al. (2015a) (square), Bouwens et al. (2015) (down-triangles), Ouchi et al. (2009) (up-triangle), Schenker et al. (2013) (pentagons), Livermore et al. (2017) (diamonds), Bradley et al. (2012) (star), and Kawamata et al. (2017) (hexagon).

result because of its large uncertainty. We also use the Q_{HII} data plotted in the right panel of Figure 9 from Bolton et al. (2011); Carilli et al. (2010); Chornock et al. (2013, 2014); Dijkstra et al. (2011); Konno et al. (2014); McGreer et al. (2011); McQuinn et al. (2007, 2008); Mesinger & Furlanetto (2008); Mesinger (2010); Ouchi et al. (2010); Ota et al. (2008); Patel et al. (2010); Totani

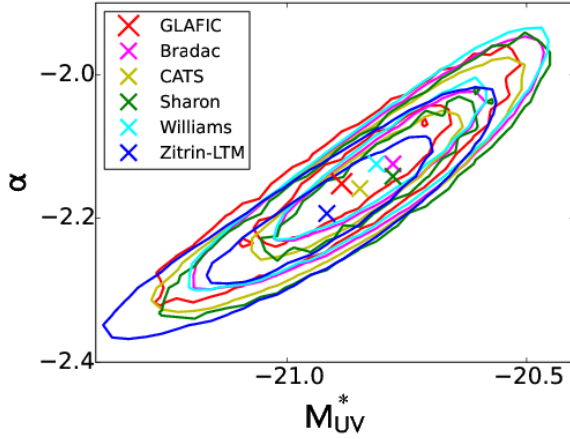


Figure 7. Contours of Schechter parameters M_* and α at $z \sim 6-7$ with different mass models; GLAFIC (red), Bradac(magenta), CATS (yellow), Sharon (green), Williams (cyan), and Zitrin-LTM (blue). The values of the best-fit Schechter parameters are shown with the cross symbols.

et al. (2006, 2014). In addition to these observational constraints, we compare $\tau_e = 0.058 \pm 0.012$ (Planck Collaboration et al. 2016) with the value of τ_e at $z = 30$ calculated from Equation (21). There are six free parameters in the χ^2 fit, $\langle f_{\text{esc}}\xi_{\text{ion}} \rangle$, M_{trunc} , and the four parameters in the function of $\rho_{\text{UV}}(z)$. The parameter range of $\langle f_{\text{esc}}\xi_{\text{ion}} \rangle$ is 0 to $10^{25.34}$ [$\text{erg}^{-1} \text{Hz}$], where we assume that $0 < f_{\text{esc}} < 1$ and $\log \xi_{\text{ion}}/\text{[erg}^{-1} \text{Hz}] = 25.34$ (Bouwens et al. 2016a). The parameter range of M_{trunc} is -16 to -10 ; $M_{\text{trunc}} = -16$ mag corresponds to the detection limit of current observations, and $M_{\text{trunc}} = -10$ mag is the magnitude of minimum halos which have star forming galaxies predicted by Faucher-Giguère et al. (2011).

We calculate the total χ^2 value by summing up the χ^2 of the data points of ρ_{UV} , Q_{HII} , and τ_e , and derive the best-fit parameters. The best-fit parameters are $\log a_p = 25.9$, $b_p = 3.7$, $c_p = 2.3$, $d_p = 5.5$, $\langle \log f_{\text{esc}}\xi_{\text{ion}} \rangle = 24.57$ and $M_{\text{trunc}} = -11.0$, and the χ^2 is 9.28 for 12 degrees of freedom. Figure 9 shows the best-fit functions of ρ_{UV} , τ_e , and Q_{HII} . These best-fit functions agree well with the data points of the observations. This result is in contrast with the conclusion of our previous study of Ishigaki et al. (2015), which claim that no parameter set can reproduce both the ρ_{UV} evolution and the value of τ_e . The main reason for this difference is that Ishigaki et al. (2015) use the value $\tau_e = 0.091^{+0.013}_{-0.014}$ from Planck Collaboration et al. (2014), which is significantly larger than the latest result used in our study ($\tau_e = 0.058 \pm 0.012$; Planck Collaboration et al. 2016). Another reason is that this study supports a non-accelerated decline of ρ_{UV} toward high redshift as explained in Section 5.1. In this study, the small value of τ_e and a non-accelerated decline of ρ_{UV} alleviate the tension between τ_e and ρ_{UV} claimed by Ishigaki et al. (2015).

Figure 10 presents the 68% and 95% confidence intervals on the $\langle f_{\text{esc}}\xi_{\text{ion}} \rangle$ - M_{trunc} plane with magenta contours. The best-fit value and the 68% interval are $\langle \log f_{\text{esc}}\xi_{\text{ion}} \rangle = 24.57^{+0.15}_{-0.08}$ and $M_{\text{trunc}} > -14.0$. If we assume $\log \xi_{\text{ion}}/\text{[erg}^{-1} \text{Hz}] = 25.34$ obtained in Bouwens et al. (2016a), we place upper and lower limits on the

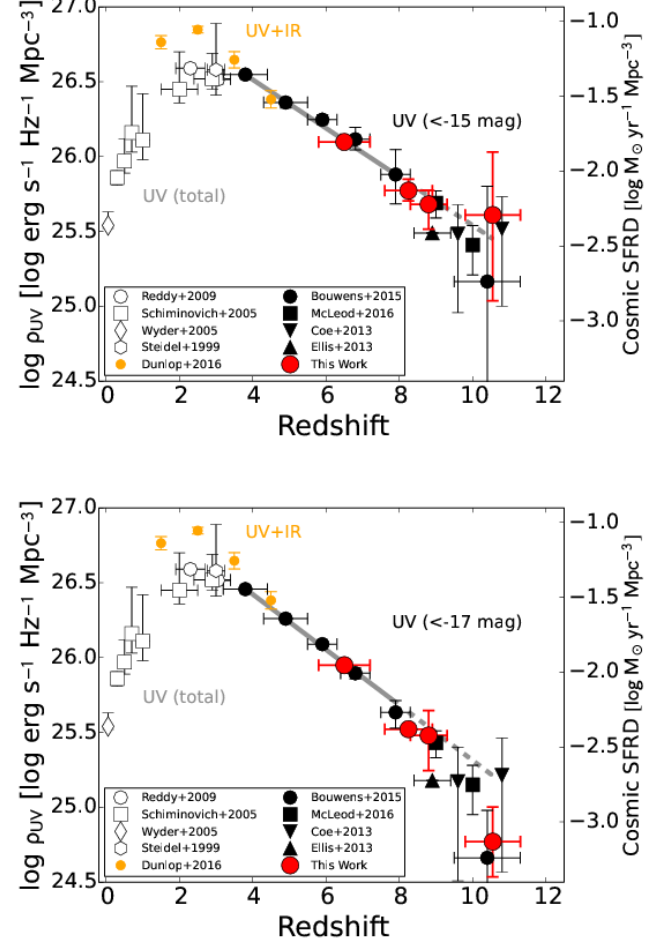


Figure 8. UV luminosity densities ρ_{UV} calculated with $M_{\text{trunc}} = -15$ (top) and $M_{\text{trunc}} = -17$ (bottom). We show ρ_{UV} taken from this work (red circles), Bouwens et al. (2015) (black filled circles), McLeod et al. (2016) (black filled squares), Coe et al. (2013) (black filled down-triangles), and Ellis et al. (2013) (black filled up-triangles). We also plot total ρ_{UV} from Steidel et al. (1999) (open hexagon), Wyder et al. (2005) (open diamond), Schiminovich et al. (2005) (open squares), and Reddy & Steidel (2009) (open circles). The orange circles denote the cosmic SFRDs derived with ρ_{UV} and IR luminosity densities (Dunlop et al. 2017). The gray solid and dashed lines show a linear fitting to samples in this work and Bouwens et al. (2015) at $z \sim 4-8$ and its extrapolation to $z \sim 8-10$, respectively.

escape fraction, $f_{\text{esc}} < 0.24$ and $f_{\text{esc}} > 0.14$, respectively. These constraints of f_{esc} and M_{trunc} are mainly driven by the observational constraints of Q_{HII} . We also derive the length of the reionization period Δz that is defined by the period bracketed by two redshifts whose Q_{HII} values are 0.1 and 0.99. Figure 10 shows the contours of Δz predicted by our χ^2 fitting results. The contours suggest $\Delta z = 3.9^{+2.0}_{-1.6}$ in the 68% confidence interval on the $\langle f_{\text{esc}}\xi_{\text{ion}} \rangle$ - M_{trunc} plane. Planck Collaboration et al. (2016) obtain $\Delta z < 2.8$ from kSZ constraints and a reionization model, which is indicative of the relatively sharp reionization history. The blue shade in Figure 10 presents the 68% confidence interval constrained from the result of Planck Collaboration et al. (2016) on the $\langle f_{\text{esc}}\xi_{\text{ion}} \rangle$ - M_{trunc} plane. Our constraints on Δz are complimentary to those of Planck Collaboration et al. (2016), giving

both the upper and lower limit of Δz . The combination of the constraints from our and Planck Collaboration et al. (2016) studies suggest $\Delta z \sim 2 - 3$, which suggests the moderately sharp reionization history.

6. SUMMARY

In this study, we have produced catalogs of dropout galaxies at $z \sim 6 - 10$ using the all cluster and parallel fields data taken by the HFF program. Using our new mass models, we have conducted Monte-Carlo simulations, and estimated the number densities of dropout galaxies at $z \sim 6 - 10$. We then derive the UV luminosity densities and discuss the properties of ionizing sources and reionization. The results in this study are summarized below:

1. With the dropout selection technique, we identify ~ 400 star-forming galaxies over the redshift range $z \sim 6 - 10$, which include 350 i -dropout, 66 Y -dropout, and 40 YJ -dropout candidates. We do not find J -dropout candidates in the HFF data. The number of dropout candidates in our catalogs is six times larger than the one obtained in our previous study (Ishigaki et al. 2015) that use one set of the cluster and parallel field data.
2. The faint end slope of UV luminosity functions has a very steep value $\alpha \sim -2$. The UV luminosity densities calculated from the UV luminosity functions are consistent with those in previous studies. Our results support the evolutionary trend of a non-accelerated decline in the UV luminosity densities beyond $z \sim 8$ in the case of $M_{\text{trunc}} = -15$, consistent with the conclusions of McLeod et al. (2016), while an accelerated decline in the case of a brighter truncation magnitude of $M_{\text{trunc}} = -17$, consistent with the conclusions of Oesch et al. (2013); Bouwens et al. (2015); Ishigaki et al. (2015); Oesch et al. (2015).
3. Using the standard analytical reionization model, we calculate the physical parameters related to reionization, such as the Thomson scattering optical depth τ_e and the ionized hydrogen fraction Q_{HII} . The values of τ_e and Q_{HII} are consistent with the latest result of Planck Collaboration et al. (2016) ($\tau_e = 0.0058 \pm 0.0012$) and previous studies of Q_{HII} obtained with Ly α absorptions found in QSOs, GRBs, and galaxies. We obtain the constraints on the parameters of ionizing sources. The best-fit value and the 68% confidence intervals of the averaged value of the escape fraction and truncation magnitude are $f_{\text{esc}} = 0.17^{+0.07}_{-0.03}$ and $M_{\text{trunc}} > -14.0$, respectively, under the assumption of $\log \xi_{\text{ion}} / [\text{erg}^{-1} \text{Hz}] = 25.34$. The results suggest that the length of the reionization period is $\Delta z = 3.9^{+2.0}_{-1.6}$ which is consistent with the Δz estimate from the kinetic Sunyaev-Zeldovich effect in Planck Collaboration et al. (2016).

We are grateful to Akio Inoue, Masayuki Umemura, Masanori Iye, Kentaro Nagamine, Takatoshi Shibuya for useful comments and discussions. This research was supported by the Munich Institute for Astro- and Particle

Physics (MIAPP) of the DFG cluster of excellence "Origin and Structure of the Universe". This work is supported by World Premier International Research Center Initiative (WPI Initiative), MEXT, Japan, and KAKENHI (JP15H02064, JP26800093, and JP15H05892) Grant-in-Aid for Scientific Research (A) through Japan Society for the Promotion of Science (JSPS). M.I. acknowledges support by Grant-in-Aid for JSPS Research Fellow (JP16J03727) and an Advanced Leading Graduate Course for Photon Science grant. R.K. acknowledges support by Grant-in-Aid for JSPS Research Fellow (JP16J01302).

Facilities: *HST* (WFC3, ACS)

REFERENCES

- Arnouts, S., Schiminovich, D., Ilbert, O., et al. 2005, ApJ, 619, L43
 Atek, H., Richard, J., Kneib, J.-P., et al. 2014, ApJ, 786, 60
 Atek, H., Richard, J., Jauzac, M., et al. 2015a, ApJ, 814, 69
 Atek, H., Richard, J., Kneib, J.-P., et al. 2015b, ApJ, 800, 18
 Bennett, C. L., Larson, D., Weiland, J. L., et al. 2013, ApJS, 208, 20
 Bernard, S. R., Carrasco, D., Trenti, M., et al. 2016, ApJ, 827, 76
 Bertin, E., & Arnouts, S. 1996, A&AS, 117, 393
 Bertin, E., Mellier, Y., Radovich, M., et al. 2002, in Astronomical Society of the Pacific Conference Series, Vol. 281, Astronomical Data Analysis Software and Systems XI, ed. D. A. Bohlander, D. Durand, & T. H. Handley, 228
 Bolton, J. S., Haehnelt, M. G., Warren, S. J., et al. 2011, MNRAS, 416, L70
 Bouwens, R. J., Illingworth, G. D., Oesch, P. A., et al. 2017a, ApJ, 843, 41
 Bouwens, R. J., Oesch, P. A., Illingworth, G. D., Ellis, R. S., & Stefanon, M. 2017b, ApJ, 843, 129
 Bouwens, R. J., Smit, R., Labb  , I., et al. 2016a, ApJ, 831, 176
 Bouwens, R. J., Illingworth, G. D., Oesch, P. A., et al. 2014, ApJ, 793, 115
 —. 2015, ApJ, 803, 34
 Bouwens, R. J., Oesch, P. A., Labb  , I., et al. 2016b, ApJ, 830, 67
 Bowler, R. A. A., Dunlop, J. S., McLure, R. J., et al. 2014, MNRAS, 440, 2810
 Brada  , M., Treu, T., Applegate, D., et al. 2009, ApJ, 706, 1201
 Bradley, L. D., Trenti, M., Oesch, P. A., et al. 2012, ApJ, 760, 108
 Calvi, V., Trenti, M., Stiavelli, M., et al. 2016, ApJ, 817, 120
 Carilli, C. L., Wang, R., Fan, X., et al. 2010, ApJ, 714, 834
 Chornock, R., Berger, E., Fox, D. B., et al. 2014, ArXiv e-prints, arXiv:1405.7400
 —. 2013, ApJ, 774, 26
 Coe, D., Bradley, L., & Zitrin, A. 2015, ApJ, 800, 84
 Coe, D., Zitrin, A., Carrasco, M., et al. 2013, ApJ, 762, 32
 Dijkstra, M., Mesinger, A., & Wyithe, J. S. B. 2011, MNRAS, 414, 2139
 Dunlop, J. S., McLure, R. J., Biggs, A. D., et al. 2017, MNRAS, 466, 861
 Ellis, R. S., McLure, R. J., Dunlop, J. S., et al. 2013, ApJ, 763, L7
 Fan, X., Strauss, M. A., Becker, R. H., et al. 2006, AJ, 132, 117
 Faucher-Gigu  re, C.-A., Kere  , D., & Ma, C.-P. 2011, MNRAS, 417, 2982
 Finkelstein, S. L., Ryan, Jr., R. E., Papovich, C., et al. 2015, ApJ, 810, 71
 Finlator, K., Oh, S. P.,   zel, F., & Dav  , R. 2012, MNRAS, 427, 2464
 Hinshaw, G., Larson, D., Komatsu, E., et al. 2013, ApJS, 208, 19
 Hoag, A., Huang, K.-H., Treu, T., et al. 2016, ApJ, 831, 182
 Iliev, I. T., Mellema, G., Pen, U.-L., et al. 2006, MNRAS, 369, 1625
 Ishigaki, M., Kawamata, R., Ouchi, M., et al. 2015, ApJ, 799, 12
 Ishigaki, M., Ouchi, M., & Harikane, Y. 2016, ApJ, 822, 5
 Iwata, I., Inoue, A. K., Matsuda, Y., et al. 2009, ApJ, 692, 1287
 Japelj, J., Vanzella, E., Fontanot, F., et al. 2017, MNRAS, 468, 389
 Jauzac, M., Richard, J., Jullo, E., et al. 2015, MNRAS, 452, 1437

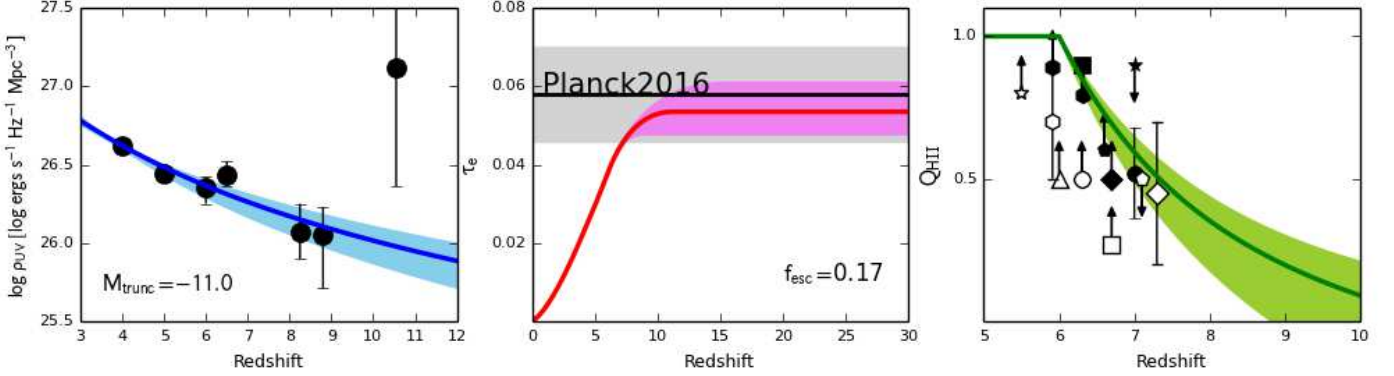


Figure 9. Left panel: ρ_{UV} calculated with $M_{\text{trunc}} = -11.0$. The black circles present ρ_{UV} from the best-fit luminosity functions at $z \sim 7 - 10$ (this work) and those at $z \sim 4 - 6$ (Bouwens et al. 2015). The blue line and the light blue shade denote the best-fit function of ρ_{UV} and the 1σ error, respectively, calculated with Equation (22) (see text for the best-fit parameters). The up-scattering $\rho_{\text{UV}}(z)$ at $z \sim 10$ due to the large uncertainty in α does not affect the fitting result, because the uncertainty in $\rho_{\text{UV}}(z)$ is also large. Middle panel: τ_e integrating from $z = 0$ to a redshift z . The red line and the magenta shade represent $\tau_e(z)$ and the 1σ error, respectively, that are consistent with $\rho_{\text{UV}}(z)$ shown with the blue line in the left panel. The black line and the gray region show the values of τ_e and its 1σ error, respectively, obtained by Planck Collaboration et al. (2016). Right panel: evolution of Q_{HII} . The green line and the light green shade present Q_{HII} and the 1σ error, respectively, that agree with $\rho_{\text{UV}}(z)$ shown with the blue line in the left panel based on Equation 16. The symbols denote constraints of Q_{HII} from Ota et al. (2008) (filled circle), Konno et al. (2014) (open diamond), Carilli et al. (2010) (filled square), Bolton et al. (2011) (filled star), McQuinn et al. (2008) (open circle), Ouchi et al. (2010) (filled diamond), McQuinn et al. (2007) (filled pentagon), Mesinger (2010) (open triangle), McGreer et al. (2011) (open star), McQuinn et al. (2007); Mesinger & Furlanetto (2008); Dijkstra et al. (2011) (open pentagon), Chornock et al. (2013, 2014) (filled hexagons), Totani et al. (2014) (open hexagon), and Patel et al. (2010) (open square).

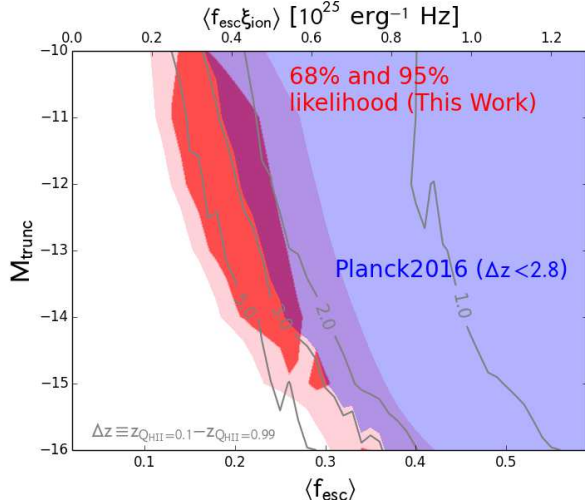


Figure 10. Contours at 68% (pink shade) and 95% (magenta shade) confidence levels of $\langle f_{\text{esc}} \xi_{\text{ion}} \rangle$ and M_{trunc} parameters. The upper horizontal axis represents $\langle f_{\text{esc}} \xi_{\text{ion}} \rangle$, and the lower horizontal axis denotes the average escape fraction $\langle f_{\text{esc}} \rangle$ under the assumption of $\log \xi_{\text{ion}} / [\text{erg}^{-1} \text{Hz}] = 25.34$ (Bouwens et al. 2016a). The blue shade shows the 68% confidence contour calculated with the constraints of Δz from Planck Collaboration et al. (2016). The solid lines represent $\Delta z = 1.0, 2.0, 3.0$, and 5.0 .

- Johnson, T. L., Sharon, K., Bayliss, M. B., et al. 2014, ApJ, 797, 48
 Kashikawa, N., Shimasaku, K., Matsuda, Y., et al. 2011, ApJ, 734, 119
 Kawamata, R., Ishigaki, M., Shimasaku, K., Oguri, M., & Ouchi, M. 2015, ApJ, 804, 103
 Kawamata, R., Ishigaki, M., Shimasaku, K., et al. 2017, ArXiv e-prints, arXiv:1710.07301
 Kawamata, R., Oguri, M., Ishigaki, M., Shimasaku, K., & Ouchi, M. 2016, ApJ, 819, 114
 Konno, A., Ouchi, M., Ono, Y., et al. 2014, ApJ, 797, 16
 Kuhlen, M., & Faucher-Giguère, C.-A. 2012, MNRAS, 423, 862
 Laporte, N., Streblyanska, A., Clement, B., et al. 2014, A&A, 562, L8

- Laporte, N., Streblyanska, A., Kim, S., et al. 2015, A&A, 575, A92
 Laporte, N., Infante, L., Troncoso Iribarren, P., et al. 2016, ApJ, 820, 98
 Livermore, R. C., Finkelstein, S. L., & Lotz, J. M. 2017, ApJ, 835, 113
 Lotz, J. M., Koekemoer, A., Coe, D., et al. 2017, ApJ, 837, 97
 Madau, P., & Dickinson, M. 2014, ARA&A, 52, 415
 Madau, P., Ferguson, H. C., Dickinson, M. E., et al. 1996, MNRAS, 283, 1388
 Madau, P., Pozzetti, L., & Dickinson, M. 1998, ApJ, 498, 106
 McGreer, I. D., Mesinger, A., & Fan, X. 2011, MNRAS, 415, 3237
 McLeod, D. J., McLure, R. J., & Dunlop, J. S. 2016, MNRAS, 459, 3812
 McLeod, D. J., McLure, R. J., Dunlop, J. S., et al. 2015, MNRAS, 450, 3032
 McLure, R. J., Dunlop, J. S., Bowler, R. A. A., et al. 2013, MNRAS, 432, 2696
 McQuinn, M., Hernquist, L., Zaldarriaga, M., & Dutta, S. 2007, MNRAS, 381, 75
 McQuinn, M., Lidz, A., Zaldarriaga, M., Hernquist, L., & Dutta, S. 2008, MNRAS, 388, 1101
 Mesinger, A. 2010, MNRAS, 407, 1328
 Mesinger, A., & Furlanetto, S. R. 2008, MNRAS, 386, 1990
 Nakajima, K., Ellis, R. S., Iwata, I., et al. 2016, ApJ, 831, L9
 Nestor, D. B., Shapley, A. E., Steidel, C. C., & Siana, B. 2011, ApJ, 736, 18
 Oesch, P. A., Bouwens, R. J., Illingworth, G. D., et al. 2015, ApJ, 808, 104
 —. 2013, ApJ, 773, 75
 —. 2014, ApJ, 786, 108
 Oguri, M. 2010, PASJ, 62, 1017
 Ono, Y., Ouchi, M., Shimasaku, K., et al. 2010, ApJ, 724, 1524
 Ono, Y., Ouchi, M., Mobasher, B., et al. 2012, ApJ, 744, 83
 Ota, K., Iye, M., Kashikawa, N., et al. 2008, ApJ, 677, 12
 Ouchi, M., Mobasher, B., Shimasaku, K., et al. 2009, ApJ, 706, 1136
 Ouchi, M., Shimasaku, K., Furusawa, H., et al. 2010, ApJ, 723, 869
 Patel, M., Warren, S. J., Mortlock, D. J., & Fynbo, J. P. U. 2010, A&A, 512, L3
 Pentericci, L., Fontana, A., Vanzella, E., et al. 2011, ApJ, 743, 132
 Pentericci, L., Vanzella, E., Fontana, A., et al. 2014, ApJ, 793, 113
 Planck Collaboration, Ade, P. A. R., Aghanim, N., et al. 2014, A&A, 571, A16

- Planck Collaboration, Adam, R., Aghanim, N., et al. 2016, A&A, 596, A108
- Postman, M., Coe, D., Benitez, N., et al. 2012, ApJS, 199, 25
- Ravindranath, S., Giavalisco, M., Ferguson, H. C., et al. 2006, ApJ, 652, 963
- Reddy, N. A., & Steidel, C. C. 2009, ApJ, 692, 778
- Robertson, B. E., Ellis, R. S., Furlanetto, S. R., & Dunlop, J. S. 2015, ApJ, 802, L19
- Robertson, B. E., Furlanetto, S. R., Schneider, E., et al. 2013, ApJ, 768, 71
- Schenker, M. A., Robertson, B. E., Ellis, R. S., et al. 2013, ApJ, 768, 196
- Schiminovich, D., Ilbert, O., Arnouts, S., et al. 2005, ApJ, 619, L47
- Schmidt, K. B., Treu, T., Trenti, M., et al. 2014, ApJ, 786, 57
- Shapley, A. E., Steidel, C. C., Pettini, M., Adelberger, K. L., & Erb, D. K. 2006, ApJ, 651, 688
- Shull, J. M., Harness, A., Trenti, M., & Smith, B. D. 2012, ApJ, 747, 100
- Sokasian, A., Abel, T., Hernquist, L., & Springel, V. 2003, MNRAS, 344, 607
- Steidel, C. C., Adelberger, K. L., Giavalisco, M., Dickinson, M., & Pettini, M. 1999, ApJ, 519, 1
- Steidel, C. C., Pettini, M., & Adelberger, K. L. 2001, ApJ, 546, 665
- Sugiura, N. 1978, Communications in Statistics - Theory and Methods, 7, 13
- Totani, T., Kawai, N., Kosugi, G., et al. 2006, PASJ, 58, 485
- Totani, T., Aoki, K., Hattori, T., et al. 2014, PASJ, 66, 63
- Treu, T., Schmidt, K. B., Trenti, M., Bradley, L. D., & Stiavelli, M. 2013, ApJ, 775, L29
- Treyer, M. A., Ellis, R. S., Milliard, B., Donas, J., & Bridges, T. J. 1998, MNRAS, 300, 303
- Wang, X., Hoag, A., Huang, K.-H., et al. 2015, ApJ, 811, 29
- Wyder, T. K., Treyer, M. A., Milliard, B., et al. 2005, ApJ, 619, L15
- Zheng, W., Shu, X., Moustakas, J., et al. 2014, ApJ, 795, 93
- Zitrin, A., Broadhurst, T., Umetsu, K., et al. 2009, MNRAS, 396, 1985
- Zitrin, A., Meneghetti, M., Umetsu, K., et al. 2013, ApJ, 762, L30
- Zitrin, A., Zheng, W., Broadhurst, T., et al. 2014, ApJ, 793, L12

APPENDIX

LISTS OF DROPOUT CANDIDATES AT $Z \sim 6 - 7, 8$, AND 9

Table 4
Dropout candidates at $z \sim 6 - 7$

ID	R.A. (J2000)	Dec (J2000)	$i_{814} - Y_{105}$	$Y_{105} - J_{125}$	J_{125}^a	μ^b	Photo- z	Reference ^c
Abell2744 Cluster								
HFF1C-2251-4556	3.593804	-30.415447	2.68 ± 0.36	0.05 ± 0.05	26.10 ± 0.04	3.64	$6.62^{+0.75}_{-0.75}$	(1), (2), (7)
HFF1C-1695-4527	3.570654	-30.414659	1.33 ± 0.10	0.11 ± 0.05	26.22 ± 0.04	1.47	$6.00^{+0.69}_{-0.69}$	(1), (2)
HFF1C-2549-3119	3.606222	-30.386644	1.07 ± 0.08	0.08 ± 0.05	26.26 ± 0.04	1.55	$5.80^{+0.67}_{-0.67}$	(1), (2), (7)
HFF1C-1930-4181	3.580452	-30.405043	> 2.36	0.17 ± 0.09	26.61 ± 0.07	4.47	$6.79^{+0.76}_{-0.76}$	(1), (2), (7)
HFF1C-2516-4570	3.604865	-30.415839	0.92 ± 0.14	0.06 ± 0.08	26.67 ± 0.06	2.84	$5.64^{+0.65}_{-0.65}$...
HFF1C-2348-3454	3.597834	-30.395961	> 2.13	0.27 ± 0.11	26.79 ± 0.08	3.31	$7.00^{+0.78}_{-0.78}$	(2), (7)
HFF1C-2178-2458	3.590761	-30.379408	0.96 ± 0.14	-0.16 ± 0.10	27.07 ± 0.08	1.68	$5.84^{+0.67}_{-0.67}$	(7)
HFF1C-2047-3526	3.585321	-30.397958	> 1.83	0.13 ± 0.15	27.19 ± 0.11	3.23	$6.75^{+0.76}_{-0.76}$	(2), (7), (10)
HFF1C-2425-4143	3.601072	-30.403991	1.11 ± 0.24	0.00 ± 0.12	27.27 ± 0.10	3.74	$5.95^{+0.68}_{-0.68}$	(1), (2), (7)
HFF1C-2414-4370	3.600619	-30.410296	> 1.97	-0.06 ± 0.13	27.29 ± 0.10	11.88	$6.39^{+0.72}_{-0.72}$	(2), (7)
HFF1C-2482-2595	3.603426	-30.383219	0.87 ± 0.14	-0.13 ± 0.12	27.30 ± 0.10	1.48	$5.78^{+0.66}_{-0.66}$	(2), (7)
HFF1C-2477-4372	3.603214	-30.410350	> 1.89	-0.03 ± 0.14	27.34 ± 0.11	4.02	$6.29^{+0.71}_{-0.71}$	(1), (2), (7), (10)
HFF1C-2230-4479	3.592944	-30.413328	1.44 ± 0.33	-0.09 ± 0.14	27.36 ± 0.11	6.80	$6.10^{+0.70}_{-0.70}$	(2), (7)
HFF1C-1845-3107	3.576889	-30.386329	> 1.45	0.13 ± 0.19	27.46 ± 0.14	8.01	$6.11^{+0.82}_{-0.70}$	(2), (7)
HFF1C-2040-4471	3.585016	-30.413084	0.86 ± 0.17	-0.24 ± 0.15	27.46 ± 0.13	2.95	$5.68^{+0.65}_{-0.73}$...
HFF1C-1911-4242	3.579635	-30.406723	1.06 ± 0.37	0.08 ± 0.20	27.53 ± 0.16	3.45	$5.58^{+0.64}_{-0.25}$...
HFF1C-2616-3070	3.609003	-30.385283	1.35 ± 0.29	-0.07 ± 0.15	27.57 ± 0.12	1.44	$6.05^{+0.69}_{-0.69}$	(2), (7)
HFF1C-2509-4337	3.604563	-30.409364	1.43 ± 0.55	0.12 ± 0.19	27.63 ± 0.14	3.12	$6.08^{+0.78}_{-0.75}$	(2), (7)
HFF1C-2274-2562	3.594752	-30.382305	0.84 ± 0.23	-0.17 ± 0.18	27.73 ± 0.15	1.85	$0.06^{+3.53}_{-0.06}$...
HFF1C-2364-4454	3.598515	-30.412612	> 1.18	0.16 ± 0.27	27.94 ± 0.19	15.56	$6.58^{+0.80}_{-1.21}$	(7)
HFF1C-1991-3429	3.582960	-30.395262	> 0.90	0.14 ± 0.28	27.97 ± 0.21	9.25	$1.28^{+5.53}_{-1.07}$	(7)
HFF1C-2172-2471	3.590518	-30.379763	> 1.36	-0.02 ± 0.26	28.10 ± 0.21	1.73	$6.11^{+0.82}_{-1.11}$	(2), (7)
Abell2744 Parallel								
HFF1P-5395-1452	3.474802	-30.362578	> 2.36	0.44 ± 0.08	26.64 ± 0.06	...	$7.30^{+0.81}_{-0.81}$...
HFF1P-5292-4021	3.470509	-30.400605	0.83 ± 0.14	0.10 ± 0.09	26.96 ± 0.07	...	$5.76^{+0.66}_{-0.66}$...
HFF1P-5793-1536	3.491387	-30.364890	> 2.19	0.42 ± 0.11	26.97 ± 0.07	...	$7.33^{+0.82}_{-0.82}$...
HFF1P-5398-1451	3.474918	-30.362542	> 1.86	0.60 ± 0.12	26.98 ± 0.08	...	$7.50^{+0.83}_{-1.52}$...
HFF1P-5535-2162	3.480642	-30.371175	1.79 ± 0.34	-0.05 ± 0.09	27.05 ± 0.07	...	$6.32^{+0.72}_{-0.72}$...
HFF1P-5701-1517	3.487575	-30.364380	1.25 ± 0.27	0.32 ± 0.13	27.19 ± 0.09	...	$5.65^{+0.65}_{-4.76}$...
HFF1P-5734-3406	3.488924	-30.394630	> 1.63	0.26 ± 0.13	27.24 ± 0.09	...	$6.75^{+0.76}_{-0.79}$...
HFF1P-5581-2176	3.482550	-30.371559	1.19 ± 0.28	0.15 ± 0.11	27.25 ± 0.09	...	$5.77^{+0.66}_{-0.93}$...
HFF1P-5615-3497	3.483960	-30.397152	1.72 ± 0.42	-0.00 ± 0.12	27.32 ± 0.10	...	$6.26^{+0.71}_{-0.71}$...
HFF1P-5221-3488	3.467582	-30.396908	> 2.01	0.13 ± 0.13	27.36 ± 0.10	...	$6.75^{+0.76}_{-0.76}$...

Table 4 — *Continued*

ID	R.A. (J2000)	Dec (J2000)	$i_{814} - Y_{105}$	$Y_{105} - J_{125}$	J_{125}^{a}	μ^{b}	Photo- z	Reference ^c
HFF1P-5748-3583	3.489520	-30.399528	> 1.68	0.05 ± 0.14	27.39 ± 0.11	...	$6.64^{+0.75}_{-0.75}$...
HFF1P-5210-3156	3.467097	-30.387686	1.30 ± 0.25	-0.26 ± 0.12	27.41 ± 0.10	...	$6.06^{+0.69}_{-0.69}$...
HFF1P-5185-3398	3.466056	-30.394409	1.10 ± 0.26	-0.02 ± 0.15	27.54 ± 0.12	...	$5.93^{+0.68}_{-0.68}$...
HFF1P-5573-2343	3.482238	-30.376221	0.94 ± 0.33	0.15 ± 0.17	27.65 ± 0.13	...	$1.26^{+3.73}_{-1.08}$...
HFF1P-4940-1588	3.455844	-30.366359	1.04 ± 0.37	-0.03 ± 0.19	27.79 ± 0.15	...	$5.60^{+0.65}_{-4.69}$...
HFF1P-5327-2576	3.471985	-30.382683	> 1.23	0.26 ± 0.21	27.84 ± 0.16	...	$6.66^{+0.82}_{-2.06}$...
HFF1P-5054-1587	3.460587	-30.366320	0.94 ± 0.39	0.03 ± 0.21	27.87 ± 0.16	...	$5.76^{+0.67}_{-1.39}$...
HFF1P-5587-3058	3.482833	-30.384961	0.97 ± 0.45	0.13 ± 0.20	27.87 ± 0.16	...	$1.08^{+5.09}_{-0.92}$...
HFF1P-5687-3584	3.486988	-30.399579	0.98 ± 0.41	-0.08 ± 0.21	27.88 ± 0.17	...	$5.89^{+0.68}_{-1.22}$...
HFF1P-5638-2369	3.484920	-30.376917	1.20 ± 0.50	0.11 ± 0.21	27.90 ± 0.16	...	$5.95^{+0.71}_{-0.74}$...
HFF1P-5691-3514	3.487148	-30.397615	1.04 ± 0.40	-0.19 ± 0.21	27.90 ± 0.17	...	$4.15^{+1.95}_{-4.04}$...
HFF1P-5429-2542	3.476220	-30.381741	> 1.47	-0.12 ± 0.21	27.98 ± 0.17	...	$5.79^{+0.80}_{-5.54}$...
HFF1P-5509-1488	3.479545	-30.363580	> 1.35	0.06 ± 0.25	28.03 ± 0.20	...	$4.68^{+0.92}_{-4.28}$...
HFF1P-5453-3095	3.477238	-30.385998	> 1.33	-0.19 ± 0.22	28.08 ± 0.19	...	$6.46^{+0.73}_{-0.73}$...
HFF1P-4938-2422	3.455763	-30.378410	> 1.18	0.08 ± 0.26	28.12 ± 0.20	...	$6.05^{+1.31}_{-5.19}$...
HFF1P-5381-3517	3.474216	-30.397703	> 1.09	0.14 ± 0.27	28.12 ± 0.21	...	$6.30^{+0.92}_{-5.76}$...
HFF1P-5566-3224	3.481928	-30.389557	> 1.36	-0.26 ± 0.23	28.12 ± 0.20	...	$6.17^{+0.70}_{-0.77}$...
HFF1P-5467-2421	3.477807	-30.378362	> 1.05	0.15 ± 0.26	28.13 ± 0.20	...	$5.75^{+1.16}_{-5.13}$...
HFF1P-5445-2223	3.476915	-30.372888	> 1.22	-0.04 ± 0.25	28.16 ± 0.20	...	$5.78^{+1.00}_{-5.17}$...
HFF1P-5588-2288	3.482859	-30.374682	0.91 ± 0.49	0.02 ± 0.27	28.24 ± 0.22	...	$1.09^{+3.70}_{-1.03}$...
MACS0416 Cluster								
HFF2C-0949-5187	64.039545	-24.088540	1.08 ± 0.11	-0.01 ± 0.05	26.37 ± 0.04	1.54	$5.88^{+0.67}_{-0.67}$	(7)
HFF2C-1148-3434	64.047846	-24.062066	1.63 ± 0.13	-0.16 ± 0.06	26.64 ± 0.05	12.31	$6.23^{+0.71}_{-0.71}$	(3), (7)
HFF2C-1131-3400	64.047138	-24.061138	0.99 ± 0.11	-0.06 ± 0.08	26.93 ± 0.07	9.89	$5.88^{+0.67}_{-0.67}$	(7)
HFF2C-0899-3404	64.037485	-24.061238	1.26 ± 0.22	-0.01 ± 0.11	27.05 ± 0.09	3.21	$6.04^{+0.69}_{-0.69}$	(3), (7)
HFF2C-0828-5386	64.034514	-24.094074	1.08 ± 0.23	0.04 ± 0.15	27.22 ± 0.12	1.50	$5.90^{+0.68}_{-0.68}$	(7)
HFF2C-0960-3425	64.040012	-24.061830	1.74 ± 0.43	0.00 ± 0.14	27.32 ± 0.11	9.53	$6.28^{+0.71}_{-0.71}$	(3), (7)
HFF2C-1147-4580	64.047818	-24.082801	> 1.85	0.23 ± 0.13	27.38 ± 0.10	1.41	$6.75^{+0.76}_{-0.76}$	(3), (7)
HFF2C-1220-3595	64.050865	-24.066531	1.04 ± 0.19	-0.07 ± 0.12	27.38 ± 0.09	3.63	$5.92^{+0.68}_{-0.68}$	(3), (7)
HFF2C-1156-3446	64.048176	-24.062404	1.55 ± 0.24	-0.18 ± 0.12	27.41 ± 0.10	15.60	$6.16^{+0.70}_{-0.70}$	(7)
HFF2C-1181-3480	64.049226	-24.063349	1.76 ± 0.29	-0.22 ± 0.13	27.46 ± 0.11	26.13	$6.27^{+0.71}_{-0.71}$	(7)
HFF2C-0768-5032	64.032020	-24.084227	0.82 ± 0.26	-0.01 ± 0.20	27.47 ± 0.16	7.55	$5.47^{+0.63}_{-5.10}$...
HFF2C-0743-3348	64.030960	-24.059683	> 1.49	0.32 ± 0.16	27.52 ± 0.11	1.75	$1.39^{+5.98}_{-0.62}$...
HFF2C-1030-3258	64.042941	-24.057182	0.87 ± 0.21	-0.16 ± 0.16	27.52 ± 0.14	2.77	$5.69^{+0.66}_{-0.66}$	(7)
HFF2C-0778-3204	64.032450	-24.055671	1.14 ± 0.31	0.03 ± 0.14	27.53 ± 0.11	1.67	$5.97^{+0.68}_{-0.68}$	(7)
HFF2C-1105-5392	64.046063	-24.094241	> 1.71	0.03 ± 0.15	27.53 ± 0.11	1.23	$6.50^{+0.74}_{-0.74}$	(7)
HFF2C-0829-5229	64.034556	-24.089700	1.22 ± 0.32	-0.03 ± 0.20	27.54 ± 0.16	1.79	$5.96^{+0.68}_{-0.91}$	(3), (7)
HFF2C-0856-4435	64.035702	-24.078765	1.07 ± 0.42	0.16 ± 0.24	27.59 ± 0.18	14.19	$1.09^{+5.11}_{-0.83}$...
HFF2C-1045-3324	64.043574	-24.059001	1.36 ± 0.33	-0.19 ± 0.17	27.59 ± 0.15	4.86	$6.06^{+0.69}_{-0.69}$...
HFF2C-0933-3382	64.038890	-24.060637	> 1.68	0.00 ± 0.20	27.66 ± 0.16	3.72	$6.41^{+0.73}_{-0.73}$	(7)
HFF2C-1051-5500	64.043800	-24.097245	1.07 ± 0.42	0.17 ± 0.18	27.71 ± 0.13	1.23	$1.29^{+5.05}_{-0.85}$	(7)
HFF2C-1330-3565	64.055425	-24.065698	0.90 ± 0.26	0.00 ± 0.17	27.77 ± 0.13	2.30	$5.75^{+0.66}_{-1.07}$...
HFF2C-1225-3594	64.051077	-24.066512	1.29 ± 0.36	0.02 ± 0.17	27.78 ± 0.13	3.53	$6.03^{+0.69}_{-0.69}$	(7)
HFF2C-1308-3431	64.054524	-24.061998	0.96 ± 0.21	-0.28 ± 0.19	27.89 ± 0.16	4.17	$5.75^{+0.66}_{-0.66}$	(7)
HFF2C-0771-3205	64.032155	-24.055706	1.03 ± 0.32	-0.31 ± 0.20	27.99 ± 0.18	1.69	$5.82^{+0.67}_{-0.92}$	(7)
HFF2C-0924-5133	64.038512	-24.087045	> 1.47	-0.36 ± 0.23	28.16 ± 0.20	1.71	$6.24^{+0.71}_{-0.95}$	(7)
MACS0416 Parallel								
HFF2P-3165-7300	64.131878	-24.125007	> 2.46	0.61 ± 0.06	26.34 ± 0.03	...	$7.52^{+0.84}_{-0.84}$...
HFF2P-2773-7107	64.115583	-24.119644	2.28 ± 0.27	0.11 ± 0.04	26.38 ± 0.03	...	$6.43^{+0.73}_{-0.73}$...
HFF2P-3552-5571	64.148027	-24.099201	> 2.41	0.51 ± 0.06	26.52 ± 0.04	...	$6.32^{+0.98}_{-0.72}$...
HFF2P-2912-7330	64.121367	-24.125856	> 2.02	0.69 ± 0.11	26.93 ± 0.06	...	$7.62^{+0.84}_{-0.84}$...
HFF2P-3660-5583	64.152506	-24.099529	0.91 ± 0.12	-0.09 ± 0.09	27.01 ± 0.07	...	$5.81^{+0.67}_{-0.67}$...
HFF2P-3011-7264	64.125486	-24.124020	1.07 ± 0.20	-0.02 ± 0.08	27.13 ± 0.07	...	$5.99^{+0.68}_{-0.68}$...
HFF2P-3514-6214	64.146433	-24.105965	2.18 ± 0.54	0.00 ± 0.09	27.15 ± 0.07	...	$6.36^{+0.72}_{-0.72}$...
HFF2P-3809-6184	64.158736	-24.105133	0.92 ± 0.15	0.01 ± 0.10	27.16 ± 0.08	...	$5.77^{+0.66}_{-0.66}$...
HFF2P-3597-6014	64.149901	-24.100414	> 1.80	0.38 ± 0.12	27.25 ± 0.08	...	$7.20^{+0.80}_{-0.80}$...
HFF2P-2796-7156	64.116513	-24.121026	1.17 ± 0.31	0.07 ± 0.14	27.64 ± 0.11	...	$5.99^{+0.68}_{-0.69}$...
HFF2P-3378-6338	64.140776	-24.109396	0.82 ± 0.28	0.10 ± 0.14	27.64 ± 0.11	...	$5.41^{+0.63}_{-0.07}$...

Table 4 — *Continued*

ID	R.A. (J2000)	Dec (J2000)	$i_{814} - Y_{105}$	$Y_{105} - J_{125}$	J_{125}^{a}	μ^{b}	Photo- z	Reference ^c
HFF2P-3253-6121	64.135552	-24.103380	> 1.41	0.12 ± 0.15	27.68 ± 0.11	...	$6.63^{+0.75}_{-0.75}$...
HFF2P-3316-7571	64.138174	-24.132532	0.81 ± 0.25	-0.25 ± 0.15	27.75 ± 0.12	...	$5.27^{+0.61}_{-0.61}$...
HFF2P-3241-7291	64.135067	-24.124757	> 1.27	0.26 ± 0.18	27.81 ± 0.12	...	$1.36^{+4.94}_{-1.21}$...
HFF2P-3084-7172	64.128511	-24.121451	1.00 ± 0.30	-0.22 ± 0.15	27.85 ± 0.13	...	$5.81^{+0.67}_{-0.67}$...
HFF2P-2909-7142	64.121231	-24.120634	> 1.48	0.18 ± 0.18	27.89 ± 0.13	...	$6.11^{+0.88}_{-0.78}$...
HFF2P-3088-5573	64.128687	-24.099262	0.91 ± 0.41	-0.02 ± 0.18	27.92 ± 0.14	...	$5.81^{+0.67}_{-0.74}$...
HFF2P-3151-6300	64.131331	-24.108356	1.40 ± 0.51	-0.21 ± 0.16	27.94 ± 0.14	...	$6.12^{+0.70}_{-0.79}$...
HFF2P-3216-6167	64.134030	-24.104666	> 1.05	0.22 ± 0.19	27.96 ± 0.14	...	$6.46^{+0.92}_{-0.40}$...
HFF2P-3429-6045	64.142896	-24.101277	> 1.42	-0.03 ± 0.18	27.96 ± 0.14	...	$6.61^{+0.75}_{-0.75}$...
HFF2P-3441-8018	64.143391	-24.133838	> 1.02	0.19 ± 0.23	28.01 ± 0.16	...	$1.28^{+5.17}_{-1.10}$...
HFF2P-3602-7428	64.150087	-24.128579	> 1.18	-0.07 ± 0.22	28.10 ± 0.17	...	$6.01^{+0.79}_{-1.36}$...
HFF2P-3418-6426	64.142432	-24.111851	> 1.12	-0.15 ± 0.26	28.37 ± 0.21	...	$1.35^{+5.41}_{-1.26}$...
MACS0717 Cluster								
HFF3C-3377-4319	109.390738	37.742218	1.09 ± 0.08	-0.07 ± 0.05	25.82 ± 0.04	62.36	$5.97^{+0.68}_{-0.68}$...
HFF3C-3817-5168	109.409066	37.754681	1.52 ± 0.10	-0.05 ± 0.04	25.96 ± 0.04	4.88	$6.20^{+0.71}_{-0.71}$	(6)
HFF3C-3785-4338	109.407728	37.742740	1.48 ± 0.11	-0.07 ± 0.05	26.06 ± 0.04	8.66	$6.18^{+0.70}_{-0.70}$	(6)
HFF3C-3928-4047	109.413667	37.734645	2.13 ± 0.29	0.03 ± 0.07	26.45 ± 0.06	14.22	$6.47^{+0.73}_{-0.73}$	(6)
HFF3C-3578-5538	109.399102	37.764959	1.57 ± 0.21	-0.00 ± 0.07	26.52 ± 0.06	6.79	$6.18^{+0.70}_{-0.70}$	(6)
HFF3C-3908-4016	109.412846	37.733795	2.09 ± 0.33	0.12 ± 0.08	26.55 ± 0.06	22.49	$6.50^{+0.74}_{-0.74}$	(6)
HFF3C-3269-5069	109.386219	37.751924	1.73 ± 0.33	0.10 ± 0.09	26.66 ± 0.07	3.10	$6.22^{+0.71}_{-0.71}$	(6)
HFF3C-3342-3294	109.389277	37.724858	1.31 ± 0.27	0.12 ± 0.10	26.84 ± 0.07	2.35	$6.03^{+0.69}_{-0.69}$	(6)
HFF3C-3145-3537	109.381053	37.731611	1.43 ± 0.26	-0.05 ± 0.09	26.87 ± 0.08	3.54	$6.13^{+0.70}_{-0.70}$	(6)
HFF3C-3047-4112	109.376996	37.736450	1.31 ± 0.22	0.08 ± 0.10	26.96 ± 0.08	4.22	$6.03^{+0.69}_{-0.69}$	(6)
HFF3C-3389-4210	109.391220	37.739172	1.17 ± 0.49	0.22 ± 0.21	27.38 ± 0.16	26.64	$5.86^{+0.98}_{-0.56}$	(6)
HFF3C-3096-5100	109.379016	37.752792	1.04 ± 0.23	-0.17 ± 0.17	27.41 ± 0.15	5.04	$5.87^{+0.67}_{-0.67}$...
HFF3C-3318-5132	109.388269	37.753667	0.82 ± 0.29	0.04 ± 0.18	27.42 ± 0.14	5.61	$5.49^{+0.64}_{-0.47}$...
HFF3C-4047-4196	109.418650	37.738793	1.19 ± 0.30	-0.15 ± 0.18	27.48 ± 0.15	9.18	$5.97^{+0.68}_{-0.68}$	(6)
HFF3C-3810-4541	109.408780	37.748379	1.15 ± 0.33	-0.01 ± 0.19	27.53 ± 0.15	58.57	$5.95^{+0.68}_{-0.68}$...
HFF3C-3585-5491	109.399393	37.763654	1.17 ± 0.46	0.18 ± 0.21	27.55 ± 0.16	7.31	$5.74^{+0.90}_{-0.19}$...
HFF3C-3411-4573	109.392135	37.749271	0.97 ± 0.36	-0.02 ± 0.21	27.60 ± 0.17	9.14	$5.60^{+0.65}_{-0.19}$...
HFF3C-2777-4506	109.365722	37.747409	> 1.44	0.20 ± 0.24	27.64 ± 0.18	4.63	$6.15^{+0.98}_{-4.99}$	(6)
HFF3C-3981-4481	109.415897	37.746722	> 1.67	-0.08 ± 0.22	27.70 ± 0.18	15.12	$6.51^{+0.74}_{-0.74}$	(6)
HFF3C-3096-4181	109.379034	37.738386	1.27 ± 0.39	-0.01 ± 0.18	27.73 ± 0.15	6.22	$6.02^{+0.69}_{-0.76}$	(6)
HFF3C-3510-5294	109.396250	37.758188	> 1.38	-0.12 ± 0.25	27.88 ± 0.21	8.62	$6.21^{+0.71}_{-1.17}$...
HFF3C-3091-4467	109.378815	37.746314	> 1.72	-0.43 ± 0.24	28.11 ± 0.22	10.29	$6.41^{+0.73}_{-0.73}$...
MACS0717 Parallel								
HFF3P-2342-9539	109.347598	37.831665	2.27 ± 0.25	0.13 ± 0.05	26.15 ± 0.04	...	$6.48^{+0.73}_{-0.73}$	(6)
HFF3P-2252-9555	109.343857	37.832091	1.61 ± 0.18	-0.04 ± 0.06	26.57 ± 0.05	...	$6.22^{+0.71}_{-0.71}$	(6)
HFF3P-1410-0378	109.308788	37.843848	> 2.06	0.41 ± 0.11	26.72 ± 0.07	...	$7.14^{+0.80}_{-0.87}$	(6)
HFF3P-2427-9379	109.351141	37.827197	2.37 ± 0.45	0.07 ± 0.08	26.72 ± 0.06	...	$6.57^{+0.74}_{-0.74}$	(6)
HFF3P-1604-9275	109.316835	37.824319	> 2.25	0.14 ± 0.09	26.84 ± 0.07	...	$6.82^{+0.77}_{-0.77}$	(6)
HFF3P-1906-8524	109.329441	37.814580	> 1.95	0.37 ± 0.10	26.86 ± 0.07	...	$7.17^{+0.80}_{-0.80}$...
HFF3P-1778-9084	109.324122	37.819016	0.84 ± 0.14	-0.10 ± 0.08	26.90 ± 0.07	...	$5.79^{+0.67}_{-0.67}$	(6)
HFF3P-1705-9266	109.321068	37.824061	1.41 ± 0.36	0.39 ± 0.10	26.91 ± 0.07	...	$5.90^{+1.14}_{-0.75}$	(6)
HFF3P-1519-8364	109.313303	37.810113	> 2.23	0.14 ± 0.09	26.96 ± 0.07	...	$6.77^{+0.76}_{-0.76}$	(6)
HFF3P-1837-9275	109.326543	37.824306	1.39 ± 0.24	-0.06 ± 0.09	26.97 ± 0.07	...	$6.10^{+0.70}_{-0.70}$	(6)
HFF3P-1881-1103	109.328390	37.852862	1.64 ± 0.26	-0.17 ± 0.09	26.98 ± 0.07	...	$6.22^{+0.71}_{-0.71}$...
HFF3P-1844-9166	109.326863	37.821291	0.83 ± 0.19	0.10 ± 0.10	27.02 ± 0.08	...	$4.58^{+1.11}_{-3.88}$...
HFF3P-1855-8526	109.327331	37.814632	0.85 ± 0.16	-0.06 ± 0.10	27.03 ± 0.08	...	$5.78^{+0.66}_{-0.66}$	(6)
HFF3P-1977-9392	109.332397	37.827567	> 2.18	0.12 ± 0.11	27.08 ± 0.08	...	$6.52^{+0.74}_{-0.74}$	(6)
HFF3P-2364-9356	109.348503	37.826577	> 1.74	0.44 ± 0.14	27.19 ± 0.09	...	$7.31^{+0.81}_{-1.22}$	(6)
HFF3P-1762-0355	109.323430	37.843220	> 1.70	0.36 ± 0.13	27.22 ± 0.09	...	$6.38^{+0.87}_{-5.23}$	(6)
HFF3P-1696-0348	109.320698	37.843017	1.16 ± 0.27	0.07 ± 0.12	27.23 ± 0.09	...	$5.87^{+0.67}_{-0.67}$...
HFF3P-1892-9418	109.328836	37.828302	> 2.00	-0.05 ± 0.12	27.24 ± 0.09	...	$6.46^{+0.73}_{-0.73}$	(6)
HFF3P-1188-9165	109.299505	37.821260	0.96 ± 0.19	-0.04 ± 0.12	27.31 ± 0.10	...	$5.84^{+0.67}_{-0.67}$...
HFF3P-1399-9233	109.308292	37.823146	0.82 ± 0.19	-0.06 ± 0.14	27.45 ± 0.11	...	$5.71^{+0.66}_{-0.66}$	(6)
HFF3P-1527-9304	109.313633	37.825128	1.38 ± 0.36	-0.10 ± 0.15	27.46 ± 0.12	...	$6.09^{+0.70}_{-0.70}$...
HFF3P-1840-9281	109.326706	37.824478	0.90 ± 0.28	0.03 ± 0.15	27.46 ± 0.12	...	$5.65^{+0.65}_{-1.21}$	(6)

Table 4 — *Continued*

ID	R.A. (J2000)	Dec (J2000)	$i_{814} - Y_{105}$	$Y_{105} - J_{125}$	J_{125}^{a}	μ^{b}	Photo- z	Reference ^c
HFF3P-1263-9215	109.302636	37.822653	> 1.96	0.03 ± 0.15	27.51 ± 0.12	...	$6.53^{+0.74}_{-0.74}$	(6)
HFF3P-1949-0448	109.331212	37.845804	1.40 ± 0.53	0.26 ± 0.18	27.55 ± 0.12	...	$5.96^{+1.12}_{-0.92}$	(6)
HFF3P-1319-0277	109.304963	37.841038	1.38 ± 0.46	0.17 ± 0.21	27.56 ± 0.16	...	$5.82^{+0.81}_{-0.54}$...
HFF3P-2208-9465	109.342009	37.829592	1.03 ± 0.31	0.08 ± 0.17	27.59 ± 0.13	...	$5.58^{+0.64}_{-0.94}$	(6)
HFF3P-1307-9251	109.304485	37.823649	1.07 ± 0.23	-0.19 ± 0.15	27.61 ± 0.13	...	$1.20^{+4.68}_{-1.06}$...
HFF3P-1477-9449	109.311563	37.829163	1.34 ± 0.56	0.27 ± 0.20	27.62 ± 0.14	...	$6.05^{+0.99}_{-1.18}$	(6)
HFF3P-1538-9217	109.314090	37.822717	> 1.30	0.33 ± 0.20	27.70 ± 0.14	...	$6.61^{+0.83}_{-0.83}$...
HFF3P-1375-9505	109.307304	37.830722	1.01 ± 0.30	0.03 ± 0.18	27.71 ± 0.14	...	$1.34^{+3.40}_{-1.29}$...
HFF3P-1373-9422	109.307223	37.828402	> 1.66	0.06 ± 0.19	27.77 ± 0.15	...	$6.48^{+0.73}_{-0.73}$	(6)
HFF3P-1489-0326	109.312054	37.842390	> 1.29	0.30 ± 0.21	27.77 ± 0.15	...	$6.92^{+0.78}_{-0.84}$	(6)
HFF3P-1810-0535	109.325457	37.848216	> 1.35	0.14 ± 0.20	27.79 ± 0.15	...	$6.83^{+0.77}_{-1.43}$	(6)
HFF3P-1151-9291	109.297969	37.824773	> 1.31	0.31 ± 0.23	27.86 ± 0.16	...	$1.36^{+5.38}_{-1.19}$...
HFF3P-1813-0035	109.325574	37.834310	0.90 ± 0.40	0.04 ± 0.22	27.87 ± 0.17	...	$5.58^{+0.64}_{-0.43}$...
HFF3P-1776-8528	109.324017	37.814689	1.15 ± 0.51	-0.05 ± 0.23	27.97 ± 0.18	...	$5.72^{+0.84}_{-0.30}$...
HFF3P-1853-9354	109.327214	37.826505	0.90 ± 0.34	-0.25 ± 0.22	27.97 ± 0.18	...	$5.60^{+0.65}_{-0.27}$...
HFF3P-2010-0108	109.333783	37.836334	0.87 ± 0.35	-0.04 ± 0.23	28.01 ± 0.18	...	$5.63^{+0.65}_{-0.06}$	(6)
HFF3P-1628-9029	109.317874	37.817496	0.87 ± 0.42	0.00 ± 0.25	28.08 ± 0.19	...	$5.64^{+0.69}_{-0.28}$...
HFF3P-1936-9052	109.330679	37.818119	0.84 ± 0.40	-0.04 ± 0.25	28.14 ± 0.20	...	$5.60^{+0.67}_{-0.23}$...
HFF3P-1494-9162	109.312291	37.821185	> 1.14	0.01 ± 0.27	28.18 ± 0.21	...	$6.30^{+0.96}_{-4.99}$...
MACS1149 Cluster								
HFF4C-4025-5027	177.417749	22.417435	> 3.48	0.57 ± 0.03	25.21 ± 0.02	1.57	$7.50^{+0.83}_{-0.83}$...
HFF4C-3888-4567	177.412018	22.415777	1.11 ± 0.05	0.12 ± 0.03	25.52 ± 0.02	1.94	$5.81^{+0.67}_{-0.67}$...
HFF4C-3321-2566	177.388388	22.382390	1.67 ± 0.15	-0.07 ± 0.05	26.21 ± 0.04	1.74	$6.27^{+0.71}_{-0.71}$...
HFF4C-3180-3434	177.382540	22.395401	0.86 ± 0.09	0.07 ± 0.06	26.30 ± 0.04	2.28	$5.72^{+0.66}_{-0.66}$...
HFF4C-3911-5079	177.412999	22.418864	2.42 ± 0.36	0.03 ± 0.06	26.34 ± 0.05	1.70	$6.47^{+0.73}_{-0.73}$...
HFF4C-3672-4342	177.403011	22.409501	1.07 ± 0.10	-0.07 ± 0.06	26.49 ± 0.05	3.68	$5.96^{+0.68}_{-0.68}$...
HFF4C-4042-4205	177.418441	22.405696	0.91 ± 0.10	-0.09 ± 0.06	26.58 ± 0.05	1.77	$5.84^{+0.67}_{-0.67}$...
HFF4C-3910-4491	177.412935	22.413642	2.26 ± 0.36	-0.19 ± 0.08	26.72 ± 0.07	1.87	$6.41^{+0.73}_{-0.73}$...
HFF4C-4042-4207	177.418456	22.405770	0.97 ± 0.12	-0.11 ± 0.08	26.77 ± 0.06	1.77	$5.87^{+0.67}_{-0.67}$...
HFF4C-4046-4231	177.418619	22.406430	1.06 ± 0.15	0.05 ± 0.08	26.81 ± 0.07	1.73	$5.94^{+0.68}_{-0.68}$...
HFF4C-3952-5014	177.414690	22.417060	> 2.16	0.07 ± 0.11	27.04 ± 0.09	1.71	$6.44^{+0.73}_{-0.73}$...
HFF4C-3906-4324	177.412777	22.409016	> 1.76	0.42 ± 0.12	27.09 ± 0.08	1.95	$7.31^{+0.81}_{-1.09}$...
HFF4C-4047-4228	177.418635	22.406343	1.13 ± 0.19	-0.04 ± 0.10	27.09 ± 0.09	1.73	$5.94^{+0.68}_{-0.68}$...
HFF4C-3705-4446	177.404410	22.412396	> 1.88	0.33 ± 0.13	27.14 ± 0.09	3.50	$6.60^{+0.75}_{-0.83}$...
HFF4C-3830-3120	177.409606	22.386668	1.77 ± 0.45	0.11 ± 0.13	27.20 ± 0.10	6.20	$6.27^{+0.71}_{-0.71}$...
HFF4C-3765-3173	177.406897	22.388148	0.98 ± 0.23	0.13 ± 0.13	27.21 ± 0.10	5.16	$5.71^{+0.66}_{-4.82}$...
HFF4C-3889-3206	177.412079	22.389059	> 1.97	0.02 ± 0.14	27.31 ± 0.11	8.53	$6.66^{+0.75}_{-0.75}$...
HFF4C-3433-2527	177.393042	22.381320	0.91 ± 0.26	0.08 ± 0.13	27.33 ± 0.10	1.76	$5.83^{+0.67}_{-0.67}$...
HFF4C-4026-3382	177.417760	22.393947	1.11 ± 0.24	-0.01 ± 0.13	27.35 ± 0.10	3.17	$5.86^{+0.67}_{-0.69}$...
HFF4C-3231-2579	177.384647	22.382754	1.23 ± 0.26	-0.23 ± 0.15	27.42 ± 0.13	1.68	$6.00^{+0.69}_{-0.69}$...
HFF4C-3134-4050	177.380590	22.401408	> 2.08	-0.03 ± 0.14	27.43 ± 0.11	2.90	$6.53^{+0.74}_{-0.74}$...
HFF4C-3191-4433	177.382991	22.412040	> 1.59	0.43 ± 0.18	27.43 ± 0.12	6.95	$7.21^{+0.81}_{-1.34}$...
HFF4C-3665-4526	177.402725	22.414615	0.84 ± 0.21	-0.08 ± 0.15	27.45 ± 0.12	5.09	$5.76^{+0.66}_{-0.66}$...
HFF4C-4076-4033	177.419863	22.400937	1.48 ± 0.47	0.26 ± 0.16	27.46 ± 0.12	2.08	$6.09^{+0.78}_{-0.70}$...
HFF4C-3760-3035	177.406675	22.384327	> 1.73	0.04 ± 0.17	27.53 ± 0.13	6.53	$6.58^{+0.74}_{-0.74}$...
HFF4C-3791-4415	177.407983	22.411538	1.54 ± 0.43	-0.02 ± 0.16	27.54 ± 0.13	2.36	$6.15^{+0.70}_{-0.70}$...
HFF4C-3894-3418	177.412259	22.394967	> 1.55	0.12 ± 0.18	27.57 ± 0.13	7.09	$6.63^{+0.75}_{-0.75}$...
HFF4C-3305-4210	177.387710	22.405836	0.89 ± 0.26	0.05 ± 0.17	27.62 ± 0.13	11.21	$5.81^{+0.67}_{-0.67}$...
HFF4C-3892-3416	177.412203	22.394890	> 1.40	0.10 ± 0.20	27.72 ± 0.15	7.26	$6.62^{+0.75}_{-0.75}$...
HFF4C-3736-5005	177.405705	22.416817	> 1.34	0.25 ± 0.22	27.76 ± 0.16	2.58	$6.54^{+0.78}_{-1.23}$...
HFF4C-4205-3155	177.425223	22.387645	1.65 ± 0.52	-0.05 ± 0.20	27.77 ± 0.16	2.26	$1.29^{+5.34}_{-0.43}$...
HFF4C-3991-3123	177.416321	22.386751	1.12 ± 0.41	0.09 ± 0.22	27.85 ± 0.18	3.56	$5.81^{+0.71}_{-4.83}$...
HFF4C-3405-3155	177.391898	22.387646	1.22 ± 0.52	0.03 ± 0.22	27.86 ± 0.16	2.38	$1.33^{+5.12}_{-1.15}$...
HFF4C-3419-3006	177.392475	22.383510	0.82 ± 0.31	-0.18 ± 0.20	27.87 ± 0.16	1.93	$5.62^{+0.65}_{-4.57}$...
HFF4C-3595-4157	177.399818	22.404384	0.84 ± 0.40	0.09 ± 0.27	27.92 ± 0.20	684.51	$0.31^{+3.68}_{-0.27}$...
HFF4C-3312-2565	177.388012	22.382380	> 1.45	-0.13 ± 0.25	27.93 ± 0.20	1.73	$6.24^{+0.72}_{-0.93}$...
HFF4C-4082-3192	177.420086	22.388672	0.89 ± 0.25	-0.31 ± 0.21	27.93 ± 0.19	3.01	$5.64^{+0.65}_{-4.95}$...
HFF4C-3225-2532	177.384407	22.381448	1.23 ± 0.44	-0.21 ± 0.25	27.95 ± 0.21	1.63	$1.35^{+4.93}_{-1.29}$...

Table 4 — *Continued*

ID	R.A. (J2000)	Dec (J2000)	$i_{814} - Y_{105}$	$Y_{105} - J_{125}$	J_{125}^{a}	μ^{b}	Photo- z	Reference ^c
HFF4C-3345-3553	177.389398	22.398695	0.93 ± 0.38	-0.08 ± 0.26	27.96 ± 0.21	6.34	$0.31^{+4.63}_{-0.26}$...
HFF4C-3282-4046	177.386778	22.401297	0.85 ± 0.24	-0.45 ± 0.22	28.06 ± 0.19	5.23	$5.63^{+0.65}_{-0.65}$...
HFF4C-3829-4199	177.409561	22.405545	> 1.09	0.01 ± 0.28	28.17 ± 0.22	2.45	$6.27^{+0.82}_{-1.57}$...
MACS1149 Parallel								
HFF4P-3938-8196	177.414121	22.305448	3.02 ± 0.40	0.26 ± 0.02	25.43 ± 0.02	...	$6.74^{+0.76}_{-0.76}$...
HFF4P-4461-7461	177.435880	22.296142	> 2.90	0.64 ± 0.04	25.82 ± 0.02	...	$7.54^{+0.84}_{-0.84}$...
HFF4P-4423-8329	177.434292	22.309154	2.89 ± 0.46	0.28 ± 0.03	25.87 ± 0.02	...	$7.13^{+0.80}_{-0.80}$...
HFF4P-3681-7168	177.403385	22.288000	1.47 ± 0.22	0.01 ± 0.06	26.46 ± 0.05	...	$6.15^{+0.70}_{-0.70}$...
HFF4P-4005-7307	177.416916	22.291875	> 2.30	0.09 ± 0.06	26.59 ± 0.05	...	$6.80^{+0.76}_{-0.76}$...
HFF4P-3742-7453	177.405922	22.295927	1.31 ± 0.19	-0.01 ± 0.06	26.64 ± 0.05	...	$6.02^{+0.69}_{-0.69}$...
HFF4P-3815-7490	177.408969	22.296968	1.27 ± 0.23	0.15 ± 0.07	26.73 ± 0.06	...	$5.94^{+0.68}_{-0.68}$...
HFF4P-4208-8047	177.425354	22.301318	1.57 ± 0.27	-0.07 ± 0.07	26.79 ± 0.06	...	$6.20^{+0.71}_{-0.71}$...
HFF4P-3678-7409	177.403268	22.294703	> 1.77	0.47 ± 0.10	26.88 ± 0.06	...	$7.16^{+0.80}_{-1.00}$...
HFF4P-3695-7381	177.403979	22.293922	> 1.75	0.44 ± 0.10	26.93 ± 0.07	...	$7.15^{+0.80}_{-1.15}$...
HFF4P-3832-7190	177.409706	22.288622	1.95 ± 0.46	0.04 ± 0.08	26.94 ± 0.07	...	$6.36^{+0.72}_{-0.72}$...
HFF4P-4539-7124	177.439130	22.286794	1.45 ± 0.24	-0.08 ± 0.09	27.14 ± 0.08	...	$6.15^{+0.70}_{-0.70}$...
HFF4P-4497-8060	177.437411	22.301678	> 1.94	0.14 ± 0.11	27.16 ± 0.08	...	$6.87^{+0.77}_{-0.77}$...
HFF4P-4269-8288	177.427882	22.308024	1.18 ± 0.28	-0.04 ± 0.10	27.17 ± 0.08	...	$6.00^{+0.69}_{-0.69}$...
HFF4P-4045-8214	177.418575	22.305965	1.30 ± 0.47	0.33 ± 0.12	27.24 ± 0.09	...	$5.81^{+1.03}_{-4.88}$...
HFF4P-4194-8047	177.424789	22.301318	1.02 ± 0.30	0.07 ± 0.11	27.27 ± 0.09	...	$5.86^{+0.67}_{-0.67}$...
HFF4P-4372-7404	177.432202	22.294557	> 1.65	0.39 ± 0.13	27.33 ± 0.09	...	$7.08^{+0.79}_{-1.21}$...
HFF4P-3881-7423	177.411719	22.295094	> 1.41	0.10 ± 0.14	27.48 ± 0.11	...	$6.75^{+0.76}_{-0.76}$...
HFF4P-4133-6595	177.422215	22.283195	1.47 ± 0.41	0.00 ± 0.13	27.48 ± 0.11	...	$6.11^{+0.70}_{-0.70}$...
HFF4P-3549-8309	177.397916	22.308605	> 1.44	0.18 ± 0.18	27.67 ± 0.13	...	$6.50^{+0.74}_{-0.83}$...
HFF4P-4005-7321	177.416898	22.292273	> 1.25	0.07 ± 0.16	27.67 ± 0.13	...	$6.62^{+0.75}_{-0.75}$...
HFF4P-4399-8595	177.433312	22.316552	> 1.33	0.02 ± 0.16	27.70 ± 0.13	...	$5.65^{+1.13}_{-0.46}$...
HFF4P-4459-7323	177.435824	22.292329	0.94 ± 0.29	-0.00 ± 0.16	27.70 ± 0.13	...	$5.44^{+0.63}_{-0.14}$...
HFF4P-3860-7488	177.410866	22.296898	0.93 ± 0.45	0.10 ± 0.17	27.73 ± 0.14	...	$5.68^{+0.85}_{-0.08}$...
HFF4P-4250-7424	177.427107	22.295124	> 1.41	-0.02 ± 0.18	27.81 ± 0.15	...	$6.47^{+0.73}_{-0.73}$...
HFF4P-4529-8297	177.438743	22.308265	> 1.35	0.07 ± 0.19	27.81 ± 0.15	...	$6.53^{+0.74}_{-0.74}$...
HFF4P-4163-8238	177.423498	22.306622	1.41 ± 0.54	-0.22 ± 0.17	27.83 ± 0.14	...	$6.09^{+0.70}_{-0.70}$...
HFF4P-3731-7203	177.405478	22.288982	> 1.29	-0.18 ± 0.20	27.84 ± 0.17	...	$6.08^{+0.69}_{-0.92}$...
HFF4P-3841-8191	177.410083	22.305310	1.03 ± 0.55	0.15 ± 0.20	27.84 ± 0.16	...	$1.32^{+4.75}_{-1.11}$...
HFF4P-4380-7515	177.432540	22.297653	0.90 ± 0.37	0.13 ± 0.20	27.87 ± 0.15	...	$1.17^{+4.70}_{-0.73}$...
HFF4P-3653-8000	177.402242	22.300011	> 1.34	0.06 ± 0.20	27.89 ± 0.16	...	$6.48^{+0.73}_{-0.73}$...
HFF4P-4110-8223	177.421272	22.306213	> 1.17	-0.04 ± 0.19	27.91 ± 0.15	...	$6.13^{+0.79}_{-1.38}$...
HFF4P-3924-7397	177.413514	22.294386	> 1.16	-0.11 ± 0.20	27.94 ± 0.16	...	$6.39^{+0.72}_{-0.82}$...
HFF4P-4417-9034	177.434056	22.317617	> 0.95	0.14 ± 0.21	27.97 ± 0.16	...	$1.27^{+4.75}_{-1.14}$...
HFF4P-3614-8432	177.400593	22.312020	> 1.13	0.15 ± 0.24	28.04 ± 0.19	...	$1.35^{+4.92}_{-1.28}$...
HFF4P-4579-7587	177.440827	22.299655	1.02 ± 0.40	-0.07 ± 0.22	28.04 ± 0.18	...	$1.26^{+4.87}_{-0.94}$...
HFF4P-4380-7427	177.432518	22.295209	> 1.35	-0.17 ± 0.24	28.19 ± 0.20	...	$6.09^{+0.70}_{-0.92}$...
AbellS1063 Cluster								
HFF5C-4581-2148	342.190894	-44.537462	1.13 ± 0.02	-0.05 ± 0.01	24.62 ± 0.01	5.99	$5.97^{+0.68}_{-0.68}$...
HFF5C-4537-1480	342.189052	-44.530026	1.12 ± 0.03	-0.01 ± 0.01	24.86 ± 0.01	4.29	$6.00^{+0.69}_{-0.69}$...
HFF5C-4111-1112	342.171301	-44.519801	1.03 ± 0.05	-0.01 ± 0.03	25.54 ± 0.02	2.47	$5.92^{+0.68}_{-0.68}$...
HFF5C-4265-2489	342.177715	-44.546931	1.41 ± 0.16	-0.01 ± 0.07	26.69 ± 0.05	3.28	$6.13^{+0.70}_{-0.70}$...
HFF5C-4159-1333	342.173329	-44.525929	1.03 ± 0.16	0.01 ± 0.08	26.76 ± 0.06	6.09	$5.92^{+0.68}_{-0.68}$...
HFF5C-4227-2335	342.176131	-44.542664	1.19 ± 0.16	-0.04 ± 0.08	26.91 ± 0.06	10.22	$6.02^{+0.69}_{-0.69}$...
HFF5C-4017-0457	342.167376	-44.512709	1.10 ± 0.24	0.18 ± 0.10	27.06 ± 0.07	1.72	$1.15^{+4.62}_{-0.53}$...
HFF5C-3822-2382	342.159275	-44.543958	> 2.14	0.06 ± 0.12	27.33 ± 0.10	4.40	$6.47^{+0.73}_{-0.73}$...
HFF5C-4877-1209	342.203210	-44.522476	> 1.62	0.31 ± 0.16	27.48 ± 0.11	8.30	$6.16^{+0.15}_{-4.88}$...
HFF5C-3944-1488	342.164364	-44.530226	1.09 ± 0.27	-0.14 ± 0.15	27.57 ± 0.12	5.87	$5.94^{+0.68}_{-0.68}$...
HFF5C-3998-0372	342.166608	-44.510345	> 1.46	0.24 ± 0.17	27.57 ± 0.12	1.60	$6.67^{+0.75}_{-0.93}$...
HFF5C-4213-1414	342.175551	-44.528186	1.31 ± 0.44	-0.04 ± 0.18	27.66 ± 0.15	58.03	$6.03^{+0.69}_{-0.75}$...
HFF5C-4186-1141	342.174445	-44.520605	> 1.23	0.15 ± 0.22	27.81 ± 0.17	3.02	$6.04^{+1.05}_{-5.51}$...
HFF5C-4650-2338	342.193770	-44.542729	0.91 ± 0.29	-0.19 ± 0.18	27.82 ± 0.15	2.55	$5.64^{+0.65}_{-5.45}$...
HFF5C-3930-1274	342.163789	-44.524303	0.89 ± 0.26	-0.21 ± 0.18	27.83 ± 0.15	2.56	$5.65^{+0.65}_{-0.65}$...
HFF5C-4509-1101	342.187910	-44.519484	0.94 ± 0.34	-0.01 ± 0.20	27.86 ± 0.16	9.31	$5.78^{+0.66}_{-0.82}$...

Table 4 — *Continued*

ID	R.A. (J2000)	Dec (J2000)	$i_{814} - Y_{105}$	$Y_{105} - J_{125}$	J_{125}^{a}	μ^{b}	Photo- z	Reference ^c
HFF5C-3913-2297	342.163049	-44.541595	1.57 ± 0.43	-0.23 ± 0.19	27.89 ± 0.16	8.72	$6.18^{+0.70}_{-0.70}$...
HFF5C-4414-2071	342.183917	-44.535313	> 1.40	-0.15 ± 0.27	27.90 ± 0.21	16.73	$6.26^{+0.71}_{-0.75}$...
HFF5C-4493-2466	342.187221	-44.546282	0.83 ± 0.31	-0.13 ± 0.20	27.92 ± 0.16	2.50	$5.58^{+0.64}_{-0.48}$...
HFF5C-3977-0487	342.165711	-44.513540	0.80 ± 0.31	-0.17 ± 0.20	27.96 ± 0.17	1.75	$5.41^{+0.63}_{-0.14}$...
HFF5C-3960-0509	342.165033	-44.514157	0.86 ± 0.35	-0.09 ± 0.21	27.97 ± 0.17	1.78	$5.66^{+0.65}_{-0.63}$...
HFF5C-4260-1364	342.177526	-44.526787	1.07 ± 0.46	-0.13 ± 0.25	28.03 ± 0.21	20.38	$5.86^{+0.70}_{-0.70}$...
HFF5C-4039-1566	342.168321	-44.532412	0.82 ± 0.40	0.03 ± 0.25	28.06 ± 0.19	51.62	$5.33^{+0.73}_{-5.11}$...
AbellS1063 Parallel								
HFF5P-1436-3153	342.309861	-44.554260	1.91 ± 0.12	0.13 ± 0.03	25.79 ± 0.02	...	$6.29^{+0.71}_{-0.71}$...
HFF5P-1475-2258	342.311461	-44.540502	1.69 ± 0.11	0.02 ± 0.03	25.88 ± 0.02	...	$6.30^{+0.71}_{-0.72}$...
HFF5P-1436-3158	342.309845	-44.554390	1.82 ± 0.13	0.16 ± 0.03	25.94 ± 0.02	...	$6.22^{+0.71}_{-0.71}$...
HFF5P-1554-3415	342.314784	-44.561532	2.25 ± 0.17	-0.20 ± 0.04	26.22 ± 0.03	...	$6.42^{+0.73}_{-0.73}$...
HFF5P-1915-3110	342.329811	-44.553074	2.60 ± 0.35	-0.10 ± 0.04	26.34 ± 0.04	...	$6.50^{+0.74}_{-0.74}$...
HFF5P-2129-2064	342.338729	-44.535120	> 2.62	0.56 ± 0.06	26.36 ± 0.04	...	$7.44^{+0.83}_{-0.83}$...
HFF5P-1929-2524	342.330388	-44.547896	> 2.74	0.17 ± 0.05	26.40 ± 0.04	...	$6.83^{+0.77}_{-0.77}$...
HFF5P-1550-3408	342.314621	-44.561337	> 3.06	-0.18 ± 0.06	26.66 ± 0.05	...	$6.47^{+0.73}_{-0.73}$...
HFF5P-1742-2148	342.322622	-44.537448	> 2.52	0.12 ± 0.06	26.69 ± 0.05	...	$6.85^{+0.77}_{-0.77}$...
HFF5P-1200-3107	342.300031	-44.552973	1.89 ± 0.27	0.11 ± 0.07	26.75 ± 0.05	...	$6.27^{+0.71}_{-0.71}$...
HFF5P-2195-1585	342.341480	-44.532925	2.07 ± 0.24	-0.26 ± 0.07	26.92 ± 0.06	...	$6.38^{+0.72}_{-0.72}$...
HFF5P-1375-1572	342.307308	-44.532566	> 1.90	0.43 ± 0.11	26.95 ± 0.07	...	$7.31^{+0.81}_{-1.67}$...
HFF5P-1545-2093	342.314400	-44.535944	2.13 ± 0.51	-0.12 ± 0.10	27.24 ± 0.08	...	$6.40^{+0.72}_{-0.73}$...
HFF5P-1587-2418	342.316159	-44.544962	0.95 ± 0.19	-0.15 ± 0.11	27.34 ± 0.09	...	$5.83^{+0.67}_{-0.67}$...
HFF5P-2100-3210	342.337526	-44.555841	1.27 ± 0.25	-0.12 ± 0.12	27.44 ± 0.10	...	$6.04^{+0.69}_{-0.69}$...
HFF5P-1653-1381	342.318877	-44.527252	1.21 ± 0.26	-0.12 ± 0.13	27.54 ± 0.11	...	$5.96^{+0.68}_{-0.68}$...
HFF5P-2357-2040	342.348226	-44.534471	1.05 ± 0.23	-0.02 ± 0.14	27.58 ± 0.11	...	$5.83^{+0.67}_{-0.67}$...
HFF5P-1200-3339	342.300002	-44.559444	1.68 ± 0.42	-0.02 ± 0.15	27.61 ± 0.12	...	$6.21^{+0.71}_{-0.71}$...
HFF5P-1512-3461	342.313006	-44.562829	> 1.84	0.09 ± 0.15	27.61 ± 0.12	...	$6.26^{+0.75}_{-0.71}$...
HFF5P-1537-2327	342.314047	-44.542428	1.21 ± 0.46	0.24 ± 0.16	27.65 ± 0.12	...	$5.82^{+1.00}_{-0.94}$...
HFF5P-1372-3301	342.307199	-44.558381	> 1.68	0.21 ± 0.17	27.68 ± 0.13	...	$6.58^{+0.74}_{-0.74}$...
HFF5P-1870-3096	342.327941	-44.552684	1.03 ± 0.43	0.19 ± 0.18	27.78 ± 0.13	...	$1.37^{+2.50}_{-1.32}$...
HFF5P-1423-3086	342.309306	-44.552397	1.78 ± 0.48	-0.20 ± 0.16	27.80 ± 0.13	...	$6.25^{+0.71}_{-0.71}$...
HFF5P-2243-2024	342.343497	-44.534020	1.03 ± 0.31	0.10 ± 0.18	27.81 ± 0.14	...	$5.86^{+0.67}_{-0.67}$...
HFF5P-1545-2521	342.314408	-44.547811	1.42 ± 0.47	-0.10 ± 0.18	27.91 ± 0.15	...	$6.11^{+0.70}_{-0.70}$...
HFF5P-1255-3099	342.302320	-44.552756	1.07 ± 0.35	0.01 ± 0.19	27.93 ± 0.15	...	$5.87^{+0.67}_{-5.07}$...
HFF5P-2068-3353	342.336177	-44.559817	> 1.38	0.03 ± 0.21	27.95 ± 0.17	...	$6.41^{+0.73}_{-5.52}$...
HFF5P-1449-2384	342.310396	-44.544023	> 1.48	-0.12 ± 0.19	27.97 ± 0.16	...	$6.12^{+0.70}_{-0.70}$...
HFF5P-2116-2400	342.338198	-44.544472	0.89 ± 0.36	0.13 ± 0.22	27.97 ± 0.17	...	$5.68^{+0.65}_{-5.49}$...
HFF5P-2227-3287	342.342824	-44.557990	0.91 ± 0.32	-0.39 ± 0.24	28.17 ± 0.22	...	$5.58^{+0.64}_{-0.65}$...
HFF5P-1957-1523	342.331570	-44.531212	1.10 ± 0.39	-0.13 ± 0.24	28.18 ± 0.20	...	$5.79^{+0.67}_{-0.71}$...
HFF5P-1908-3457	342.329506	-44.562705	0.92 ± 0.50	0.11 ± 0.26	28.19 ± 0.21	...	$0.27^{+5.83}_{-0.20}$...
HFF5P-1949-2315	342.331243	-44.542096	0.95 ± 0.39	-0.12 ± 0.24	28.20 ± 0.20	...	$5.64^{+0.69}_{-5.16}$...
HFF5P-1940-3315	342.330870	-44.558773	0.94 ± 0.54	0.16 ± 0.27	28.21 ± 0.21	...	$5.66^{+1.16}_{-5.11}$...
HFF5P-1716-2450	342.321503	-44.545838	0.96 ± 0.48	0.05 ± 0.25	28.22 ± 0.20	...	$5.66^{+0.80}_{-5.37}$...
HFF5P-2055-2411	342.335663	-44.544752	> 1.16	0.03 ± 0.27	28.25 ± 0.21	...	$1.36^{+3.06}_{-1.31}$...
HFF5P-1992-3212	342.333018	-44.555916	> 1.07	-0.02 ± 0.26	28.26 ± 0.21	...	$6.45^{+0.73}_{-1.04}$...
HFF5P-1226-3152	342.301115	-44.554238	1.05 ± 0.44	-0.09 ± 0.25	28.27 ± 0.21	...	$5.87^{+0.67}_{-1.29}$...
HFF5P-1542-1441	342.314282	-44.528924	> 1.10	0.07 ± 0.27	28.29 ± 0.22	...	$5.93^{+0.93}_{-5.29}$...
Abell370 Cluster								
HFF6C-5526-4003	39.980271	-1.566761	0.92 ± 0.07	-0.12 ± 0.07	26.11 ± 0.06	13.34	$5.85^{+0.67}_{-0.67}$...
HFF6C-5522-4002	39.980113	-1.566731	0.85 ± 0.08	-0.26 ± 0.09	26.48 ± 0.08	12.40	$5.75^{+0.66}_{-0.66}$...
HFF6C-5715-4130	39.988155	-1.570302	0.81 ± 0.15	0.05 ± 0.14	26.72 ± 0.11	3.36	$5.42^{+0.63}_{-1.08}$...
HFF6C-5659-4166	39.985811	-1.571303	1.50 ± 0.24	-0.01 ± 0.14	26.76 ± 0.11	4.35	$6.16^{+0.70}_{-0.70}$...
HFF6C-4926-4158	39.955258	-1.571082	0.88 ± 0.14	0.06 ± 0.11	26.77 ± 0.10	3.62	$5.83^{+0.67}_{-0.67}$...
HFF6C-5262-3591	39.969255	-1.566441	1.39 ± 0.27	-0.28 ± 0.17	27.09 ± 0.15	4.21	$6.09^{+0.70}_{-0.70}$...
HFF6C-5001-4358	39.958395	-1.576620	1.69 ± 0.43	-0.27 ± 0.23	27.60 ± 0.21	4.26	$6.19^{+0.70}_{-0.70}$...
Abell370 Parallel								
HFF6P-1557-6475	40.064896	-1.613212	1.47 ± 0.02	0.11 ± 0.01	24.41 ± 0.01	...	$6.05^{+0.69}_{-0.69}$...

Table 4 — *Continued*

ID	R.A. (J2000)	Dec (J2000)	$i_{814} - Y_{105}$	$Y_{105} - J_{125}$	J_{125}^{a}	μ^{b}	Photo- z	Reference ^c
HFF6P-1405-7142	40.058557	-1.620629	3.55 ± 0.44	0.28 ± 0.02	25.23 ± 0.01	...	$7.14^{+0.80}_{-0.80}$...
HFF6P-1422-8041	40.059266	-1.634499	1.83 ± 0.13	0.04 ± 0.03	25.84 ± 0.02	...	$6.27^{+0.71}_{-0.71}$...
HFF6P-1512-7449	40.063019	-1.629157	2.07 ± 0.18	0.05 ± 0.03	25.96 ± 0.03	...	$6.41^{+0.73}_{-0.73}$...
HFF6P-1066-7101	40.044450	-1.619499	1.31 ± 0.10	0.02 ± 0.04	26.26 ± 0.04	...	$6.01^{+0.69}_{-0.69}$...
HFF6P-1553-6472	40.064711	-1.613127	1.88 ± 0.23	0.21 ± 0.05	26.37 ± 0.04	...	$6.32^{+0.72}_{-0.72}$...
HFF6P-0962-7254	40.040085	-1.623733	1.43 ± 0.12	-0.10 ± 0.05	26.47 ± 0.04	...	$6.15^{+0.70}_{-0.70}$...
HFF6P-1112-8152	40.046339	-1.637564	1.10 ± 0.13	0.16 ± 0.06	26.60 ± 0.05	...	$5.19^{+0.67}_{-0.61}$...
HFF6P-1365-7298	40.056894	-1.624969	1.03 ± 0.17	0.09 ± 0.07	26.84 ± 0.06	...	$1.06^{+0.61}_{-0.61}$...
HFF6P-1338-7507	40.055776	-1.630760	2.21 ± 0.44	0.05 ± 0.08	26.90 ± 0.06	...	$6.45^{+0.73}_{-0.73}$...
HFF6P-1443-8334	40.060155	-1.642617	1.03 ± 0.16	-0.14 ± 0.09	27.04 ± 0.07	...	$5.89^{+0.68}_{-0.68}$...
HFF6P-1496-6574	40.062337	-1.615954	> 1.95	0.29 ± 0.10	27.07 ± 0.08	...	$7.11^{+0.80}_{-0.79}$...
HFF6P-1135-6350	40.047325	-1.609738	> 1.87	0.34 ± 0.11	27.11 ± 0.08	...	$6.30^{+0.84}_{-0.72}$...
HFF6P-1233-7093	40.051408	-1.619257	> 2.18	0.04 ± 0.10	27.12 ± 0.08	...	$6.51^{+0.74}_{-0.74}$...
HFF6P-1242-7083	40.051751	-1.618991	1.74 ± 0.36	-0.04 ± 0.10	27.17 ± 0.08	...	$6.30^{+0.71}_{-0.72}$...
HFF6P-1203-7168	40.050146	-1.621357	> 1.94	0.21 ± 0.11	27.18 ± 0.08	...	$6.50^{+0.74}_{-1.08}$...
HFF6P-0954-7261	40.039781	-1.623927	1.39 ± 0.25	-0.09 ± 0.11	27.29 ± 0.09	...	$6.11^{+0.70}_{-0.70}$...
HFF6P-1339-7197	40.055809	-1.622150	1.74 ± 0.46	0.01 ± 0.12	27.39 ± 0.10	...	$6.29^{+0.71}_{-0.71}$...
HFF6P-1619-8043	40.067498	-1.634549	1.61 ± 0.49	0.20 ± 0.13	27.42 ± 0.10	...	$6.20^{+0.71}_{-0.71}$...
HFF6P-1406-8067	40.058588	-1.635205	> 1.95	-0.10 ± 0.12	27.43 ± 0.10	...	$6.49^{+0.73}_{-0.73}$...
HFF6P-1120-6563	40.046698	-1.615649	> 1.69	0.19 ± 0.14	27.47 ± 0.11	...	$6.28^{+0.76}_{-0.71}$...
HFF6P-1404-6507	40.058514	-1.614092	1.12 ± 0.25	-0.09 ± 0.14	27.52 ± 0.12	...	$5.94^{+0.68}_{-0.68}$...
HFF6P-1111-8294	40.046301	-1.641520	1.34 ± 0.29	-0.14 ± 0.14	27.53 ± 0.12	...	$6.05^{+0.69}_{-0.69}$...
HFF6P-1650-7475	40.068770	-1.629867	1.36 ± 0.38	-0.16 ± 0.16	27.75 ± 0.14	...	$6.09^{+0.70}_{-0.70}$...
HFF6P-0940-7273	40.039181	-1.624272	1.52 ± 0.35	-0.33 ± 0.16	27.76 ± 0.14	...	$6.14^{+0.70}_{-0.70}$...
HFF6P-1631-7409	40.067987	-1.628035	1.55 ± 0.48	-0.12 ± 0.17	27.77 ± 0.14	...	$6.16^{+0.70}_{-0.70}$...
HFF6P-1513-6504	40.063047	-1.614000	1.15 ± 0.33	-0.09 ± 0.17	27.78 ± 0.15	...	$5.89^{+0.68}_{-0.68}$...
HFF6P-1282-8053	40.053420	-1.634833	0.88 ± 0.29	-0.10 ± 0.18	27.87 ± 0.15	...	$5.79^{+0.67}_{-0.67}$...
HFF6P-0963-7467	40.040146	-1.629650	> 1.51	0.12 ± 0.20	27.89 ± 0.16	...	$6.48^{+0.73}_{-0.97}$...
HFF6P-1352-6549	40.056353	-1.615251	> 1.13	0.22 ± 0.22	27.95 ± 0.17	...	$6.00^{+0.53}_{-0.53}$...
HFF6P-1352-8104	40.056373	-1.636246	1.05 ± 0.36	-0.21 ± 0.20	28.00 ± 0.18	...	$5.68^{+0.65}_{-0.80}$...
HFF6P-1636-7324	40.068190	-1.625671	> 1.36	-0.00 ± 0.21	28.00 ± 0.17	...	$6.45^{+0.73}_{-0.76}$...
HFF6P-1197-8268	40.049891	-1.640781	> 1.65	-0.22 ± 0.21	28.02 ± 0.19	...	$6.41^{+0.73}_{-0.73}$...
HFF6P-1485-8415	40.061875	-1.644873	0.88 ± 0.38	-0.04 ± 0.22	28.03 ± 0.18	...	$5.67^{+0.65}_{-1.66}$...
HFF6P-1346-7336	40.056107	-1.626010	> 1.06	0.18 ± 0.23	28.04 ± 0.18	...	$6.07^{+0.82}_{-0.81}$...
HFF6P-1534-8390	40.063919	-1.644193	1.09 ± 0.46	-0.05 ± 0.22	28.04 ± 0.18	...	$5.74^{+0.70}_{-5.48}$...
HFF6P-1105-8129	40.046060	-1.636943	0.98 ± 0.40	-0.01 ± 0.24	28.08 ± 0.20	...	$5.67^{+0.65}_{-4.66}$...
HFF6P-1437-6560	40.059896	-1.615568	0.91 ± 0.41	-0.08 ± 0.24	28.12 ± 0.20	...	$5.76^{+0.66}_{-4.85}$...
HFF6P-1197-8275	40.049900	-1.640994	> 1.42	-0.13 ± 0.25	28.16 ± 0.22	...	$6.21^{+0.71}_{-0.71}$...
HFF6P-1554-7558	40.064752	-1.632167	0.81 ± 0.39	-0.14 ± 0.24	28.20 ± 0.21	...	$1.17^{+3.86}_{-1.06}$...

^a Total magnitudes m_{tot} estimated with the aperture correction $m_{\text{tot}} = m_{\text{AP}} - 0.82$.^b Magnifications calculated with mass models in Kawamata et al. (2017).^c References. (1)Atek et al. (2014), (2)Atek et al. (2015a), (3)Coe et al. (2015), (4)Laporte et al. (2014), (5)Laporte et al. (2015), (6)Laporte et al. (2016), (7)Livermore et al. (2017), (8)McLeod et al. (2016), (9)Oesch et al. (2015) (10)Zheng et al. (2014), (11)Zitrin et al. (2014)**Table 5**
Dropout candidates at $z \sim 8$

ID	R.A. (J2000)	Dec (J2000)	$Y_{105} - J_{125}$	$J_{125} - JH_{140}$	JH_{140}^{a}	μ^{b}	Photo- z	Reference ^c
Abell2744 Cluster								
HFF1C-2508-2496	3.604518	-30.380467	1.17 ± 0.07	0.04 ± 0.04	25.92 ± 0.03	1.31	$8.00^{+0.88}_{-0.88}$	(1), (2), (3), (4), (10)
HFF1C-2481-2561	3.603378	-30.382254	1.27 ± 0.15	0.14 ± 0.08	26.64 ± 0.05	1.40	$8.20^{+0.90}_{-0.90}$	(2), (3), (7), (10)
HFF1C-2306-3089	3.596091	-30.385833	1.30 ± 0.16	0.06 ± 0.08	26.68 ± 0.06	2.04	$8.18^{+0.90}_{-0.90}$	(2), (3), (7), (10)
HFF1C-2555-2515	3.606461	-30.380996	1.12 ± 0.14	-0.18 ± 0.09	26.95 ± 0.07	1.33	$7.96^{+0.88}_{-0.88}$	(2), (3), (7), (10)
HFF1C-2492-2561	3.603859	-30.382263	1.92 ± 0.37	0.16 ± 0.11	26.99 ± 0.07	1.40	$8.40^{+0.92}_{-0.92}$	(2), (3), (7), (8), (10)
HFF1C-2557-2513	3.606577	-30.380924	1.10 ± 0.24	0.22 ± 0.13	27.17 ± 0.08	1.32	$7.88^{+0.87}_{-6.13}$	(2), (10)
HFF1C-2135-2432	3.588980	-30.378668	1.13 ± 0.19	-0.19 ± 0.13	27.30 ± 0.10	1.69	$7.94^{+0.88}_{-0.88}$	(2), (3), (10)
HFF1C-2495-2562	3.603997	-30.382304	1.05 ± 0.32	0.13 ± 0.19	27.61 ± 0.12	1.40	$7.90^{+0.87}_{-6.08}$	(10)
HFF1C-2216-4356	3.592349	-30.409892	0.60 ± 0.28	-0.30 ± 0.25	28.01 ± 0.20	8.56	$7.22^{+0.81}_{-2.02}$	(2), (7), (10)

Table 5 — *Continued*

ID	R.A. (J2000)	Dec (J2000)	$Y_{105} - J_{125}$	$J_{125} - JH_{140}$	JH_{140}^a	μ^b	Photo- z	Reference ^c
HFF1C-2521-2532	3.605062	-30.381463	0.84 ± 0.32	-0.16 ± 0.25	28.07 ± 0.18	1.35	$7.67^{+0.85}_{-6.39}$	(2), (7)
Abell2744 Parallel								
HFF1P-5398-1451	3.474918	-30.362542	0.60 ± 0.12	-0.05 ± 0.11	27.03 ± 0.08	...	$7.50^{+0.83}_{-1.52}$...
HFF1P-5021-2024	3.459245	-30.367360	0.70 ± 0.20	-0.06 ± 0.17	27.53 ± 0.12	...	$7.56^{+0.84}_{-1.80}$...
HFF1P-5512-1588	3.479684	-30.366359	0.86 ± 0.36	0.21 ± 0.25	27.81 ± 0.15	...	$7.76^{+0.86}_{-6.38}$...
HFF1P-5530-3153	3.480419	-30.387608	0.55 ± 0.25	0.08 ± 0.22	27.84 ± 0.15	...	$7.28^{+0.81}_{-6.27}$...
MACS0416 Cluster								
HFF2C-1151-4540	64.047984	-24.081670	1.92 ± 0.20	0.01 ± 0.06	26.50 ± 0.04	1.44	$8.39^{+0.92}_{-0.92}$	(3), (5), (8)
HFF2C-0939-5354	64.039164	-24.093183	2.19 ± 0.34	0.18 ± 0.08	26.61 ± 0.05	1.38	$8.50^{+0.93}_{-0.93}$	(5), (8)
HFF2C-1153-4531	64.048057	-24.081431	2.28 ± 0.56	0.49 ± 0.11	26.80 ± 0.06	1.44	$8.67^{+0.95}_{-0.95}$	(3), (5)
HFF2C-0901-5171	64.037567	-24.088109	1.94 ± 0.63	0.12 ± 0.18	27.56 ± 0.12	1.70	$8.36^{+0.92}_{-0.92}$	(5), (7), (8)
HFF2C-1447-3538	64.060329	-24.064958	0.86 ± 0.19	-0.31 ± 0.16	27.71 ± 0.12	1.79	$7.70^{+0.85}_{-0.85}$	(7)
MACS0416 Parallel								
HFF2P-2912-7330	64.121367	-24.125856	0.69 ± 0.11	-0.14 ± 0.09	27.07 ± 0.06	...	$7.62^{+0.84}_{-0.84}$...
HFF2P-3286-6419	64.136930	-24.111643	0.98 ± 0.18	0.13 ± 0.10	27.21 ± 0.06	...	$7.81^{+0.86}_{-0.86}$...
HFF2P-3596-6480	64.149865	-24.113353	1.74 ± 0.58	0.39 ± 0.17	27.56 ± 0.09	...	$8.52^{+0.93}_{-0.93}$	(3), (8)
HFF2P-3044-6002	64.126862	-24.100067	1.20 ± 0.27	-0.21 ± 0.16	27.80 ± 0.12	...	$1.76^{+6.42}_{-0.27}$	(8)
HFF2P-3042-6011	64.126779	-24.100323	1.33 ± 0.43	0.18 ± 0.19	27.81 ± 0.12	...	$8.19^{+0.90}_{-0.94}$	(3), (8)
HFF2P-3549-6422	64.147904	-24.111729	2.26 ± 0.97	-0.02 ± 0.21	28.02 ± 0.14	...	$8.35^{+0.92}_{-0.92}$...
HFF2P-2862-7348	64.119271	-24.126357	0.78 ± 0.31	-0.09 ± 0.23	28.07 ± 0.16	...	$5.74^{+2.19}_{-5.18}$...
HFF2P-3642-6304	64.151758	-24.108450	> 2.04	0.15 ± 0.27	28.13 ± 0.17	...	$8.61^{+0.94}_{-6.48}$	(3), (8)
HFF2P-2871-7010	64.119662	-24.116955	0.86 ± 0.31	-0.12 ± 0.22	28.14 ± 0.16	...	$7.69^{+0.85}_{-6.20}$...
MACS0717 Parallel								
HFF3P-2251-9452	109.343797	37.829234	1.35 ± 0.33	0.21 ± 0.15	27.26 ± 0.10	...	$8.25^{+0.91}_{-0.91}$	(6)
HFF3P-1788-9254	109.324524	37.823744	1.26 ± 0.27	-0.05 ± 0.15	27.37 ± 0.10	...	$8.06^{+0.89}_{-0.89}$	(6)
HFF3P-1891-8538	109.328823	37.814951	0.61 ± 0.19	-0.19 ± 0.17	27.62 ± 0.13	...	$5.51^{+1.66}_{-4.87}$	(6)
HFF3P-1672-0089	109.319676	37.835808	0.54 ± 0.24	-0.01 ± 0.20	27.67 ± 0.14	...	$7.29^{+0.81}_{-2.33}$...
HFF3P-1854-0446	109.327261	37.845741	0.92 ± 0.33	-0.09 ± 0.24	27.93 ± 0.18	...	$7.76^{+2.74}_{-5.86}$...
HFF3P-2153-9369	109.339742	37.826923	0.95 ± 0.34	-0.11 ± 0.25	27.95 ± 0.18	...	$7.76^{+0.86}_{-6.00}$	(6)
MACS1149 Cluster								
HFF4C-4025-5027	177.417749	22.417435	0.57 ± 0.03	0.02 ± 0.02	25.19 ± 0.02	1.57	$7.50^{+0.83}_{-0.83}$...
HFF4C-4024-4492	177.417702	22.413687	1.61 ± 0.50	0.35 ± 0.19	27.26 ± 0.12	1.63	$8.42^{+0.92}_{-0.92}$...
MACS1149 Parallel								
HFF4P-3745-6484	177.406060	22.280113	1.71 ± 0.29	0.36 ± 0.10	26.66 ± 0.06	...	$8.37^{+0.92}_{-0.92}$...
HFF4P-3998-8560	177.416587	22.315557	1.16 ± 0.15	0.07 ± 0.09	26.85 ± 0.06	...	$7.96^{+0.88}_{-0.88}$...
HFF4P-3959-8115	177.414974	22.303195	0.63 ± 0.16	-0.00 ± 0.14	27.36 ± 0.09	...	$7.53^{+0.84}_{-2.07}$...
HFF4P-3612-8473	177.400509	22.313149	0.68 ± 0.19	-0.03 ± 0.16	27.55 ± 0.11	...	$7.57^{+0.84}_{-6.25}$...
HFF4P-4149-8180	177.422903	22.305006	0.83 ± 0.23	0.02 ± 0.18	27.67 ± 0.12	...	$7.73^{+0.86}_{-6.66}$...
HFF4P-3769-8456	177.407054	22.312680	0.60 ± 0.20	-0.17 ± 0.19	27.78 ± 0.14	...	$7.38^{+0.82}_{-1.50}$...
HFF4P-4419-8349	177.434162	22.309708	0.76 ± 0.23	-0.28 ± 0.21	27.98 ± 0.17	...	$1.71^{+6.08}_{-1.19}$...
HFF4P-3878-7079	177.411594	22.285550	1.02 ± 0.40	0.04 ± 0.25	28.01 ± 0.17	...	$7.86^{+0.87}_{-6.63}$...
HFF4P-4553-7304	177.439740	22.291792	0.78 ± 0.32	0.02 ± 0.24	28.01 ± 0.17	...	$7.54^{+0.84}_{-6.48}$...
HFF4P-3593-8440	177.399737	22.312238	0.79 ± 0.28	-0.31 ± 0.25	28.15 ± 0.19	...	$7.45^{+0.83}_{-6.68}$...
AbellS1063 Cluster								
HFF5C-4316-1323	342.179848	-44.525661	1.48 ± 0.26	0.08 ± 0.11	26.97 ± 0.08	27.72	$8.21^{+0.90}_{-0.90}$...
HFF5C-4374-1338	342.182266	-44.526074	1.88 ± 0.57	0.35 ± 0.16	27.21 ± 0.09	24.75	$8.52^{+0.93}_{-0.93}$...
HFF5C-4111-2125	342.171304	-44.536810	0.54 ± 0.23	-0.22 ± 0.22	27.60 ± 0.17	4.10	$1.64^{+1.52}_{-0.87}$...
HFF5C-3935-1469	342.163986	-44.529704	1.06 ± 0.41	0.15 ± 0.25	27.89 ± 0.16	5.13	$7.92^{+0.87}_{-6.93}$...
AbellS1063 Parallel								
HFF5P-2129-2064	342.338729	-44.535120	0.56 ± 0.06	0.03 ± 0.05	26.33 ± 0.03	...	$7.44^{+0.83}_{-0.83}$...
HFF5P-1912-1491	342.329688	-44.530307	0.96 ± 0.10	-0.04 ± 0.07	26.75 ± 0.05	...	$7.88^{+0.87}_{-0.87}$...
HFF5P-1278-2047	342.303254	-44.534661	1.17 ± 0.45	0.16 ± 0.24	27.85 ± 0.15	...	$7.98^{+0.88}_{-6.34}$...
HFF5P-2027-2472	342.334489	-44.546470	0.55 ± 0.21	-0.27 ± 0.21	28.07 ± 0.15	...	$7.21^{+0.81}_{-6.07}$...
HFF5P-1617-1544	342.317413	-44.531796	0.80 ± 0.34	-0.08 ± 0.25	28.19 ± 0.18	...	$1.75^{+5.27}_{-1.46}$...
HFF5P-1222-3093	342.300944	-44.552588	1.09 ± 0.41	-0.08 ± 0.25	28.20 ± 0.17	...	$7.88^{+0.87}_{-6.46}$...

Table 5 — *Continued*

ID	R.A. (J2000)	Dec (J2000)	$Y_{105} - J_{125}$	$J_{125} - JH_{140}$	JH_{140}^{a}	μ^{b}	Photo- z	Reference ^c
Abell370 Cluster								
HFF6C-5058-4269	39.960762	-1.574159	0.83 ± 0.05	-0.06 ± 0.04	25.62 ± 0.03	8.65	$7.78^{+0.86}_{-0.86}$...
HFF6C-5131-4097	39.963821	-1.569362	0.96 ± 0.09	-0.07 ± 0.07	25.99 ± 0.05	8.93	$7.88^{+0.87}_{-0.87}$...
HFF6C-5578-4519	39.982425	-1.581097	1.63 ± 0.22	-0.04 ± 0.10	26.49 ± 0.07	8.05	$8.23^{+0.90}_{-0.90}$...
HFF6C-5420-5141	39.975874	-1.587261	1.78 ± 0.35	-0.08 ± 0.15	26.93 ± 0.11	4.66	$8.22^{+0.90}_{-0.90}$...
HFF6C-4926-4404	39.955279	-1.577912	2.03 ± 0.47	0.02 ± 0.16	26.98 ± 0.11	3.16	$8.34^{+0.92}_{-0.92}$...
HFF6C-5187-5411	39.966133	-1.594771	0.61 ± 0.27	0.07 ± 0.24	27.34 ± 0.16	17.57	$7.38^{+0.82}_{-5.89}$...
Abell370 Parallel								
HFF6P-1733-6559	40.072227	-1.615552	0.78 ± 0.23	0.19 ± 0.17	27.49 ± 0.11	...	$7.58^{+0.84}_{-2.15}$...
HFF6P-1374-7002	40.057265	-1.616732	0.69 ± 0.27	-0.04 ± 0.24	27.97 ± 0.17	...	$1.64^{+6.17}_{-0.54}$...
HFF6P-1167-6515	40.048638	-1.614306	0.66 ± 0.33	-0.08 ± 0.30	28.25 ± 0.22	...	$1.77^{+1.36}_{-1.56}$...

^a Total magnitudes m_{tot} estimated with the aperture correction $m_{\text{tot}} = m_{\text{AP}} - 0.82$.

^b Magnifications calculated with mass models in Kawamata et al. (2017).

^c References. (1)Atek et al. (2014), (2)Atek et al. (2015a), (3)Coe et al. (2015), (4)Laporte et al. (2014), (5)Laporte et al. (2015), (6)Laporte et al. (2016), (7)Livermore et al. (2017), (8)McLeod et al. (2016), (9)Oesch et al. (2015) (10)Zheng et al. (2014), (11)Zitrin et al. (2014)

Table 6
Dropout candidates at $z \sim 9$

Table 6 — *Continued*

ID	R.A. (J2000)	Dec (J2000)	$YJ - JH_{140}$	$JH_{140} - H_{160}$	H_{160}^{a}	μ^{b}	Photo- z	Reference ^c
HFF5C-4316-1323	342.179874	-44.525660	0.78 ± 0.12	-0.03 ± 0.12	27.07 ± 0.08	29.58	$8.15^{+0.90}_{-0.90}$...
HFF5C-4374-1338	342.182264	-44.526074	1.29 ± 0.16	-0.13 ± 0.14	27.34 ± 0.11	24.15	$8.52^{+0.93}_{-0.93}$...
AbellS1063 Parallel								
HFF5P-1975-2112	342.332299	-44.536446	1.05 ± 0.23	0.21 ± 0.16	27.47 ± 0.10	...	$2.13^{+6.51}_{-0.45}$...
HFF5P-2042-2369	342.335117	-44.543602	0.94 ± 0.36	0.17 ± 0.30	28.20 ± 0.20	...	$8.29^{+1.01}_{-6.63}$...
HFF5P-2092-3100	342.337186	-44.552795	> 0.94	0.00 ± 0.32	28.42 ± 0.24	...	$8.19^{+0.90}_{-2.43}$...
Abell370 Cluster								
HFF6C-5578-4519	39.982427	-1.581097	0.78 ± 0.10	0.04 ± 0.10	26.45 ± 0.06	8.26	$8.23^{+0.90}_{-0.90}$...
HFF6C-5421-5141	39.975875	-1.587260	0.81 ± 0.15	-0.07 ± 0.15	27.01 ± 0.10	4.55	$8.23^{+0.90}_{-0.90}$...
Abell370 Parallel								
HFF6P-1732-6562	40.072207	-1.615618	0.85 ± 0.17	0.03 ± 0.15	27.43 ± 0.10	...	$8.14^{+0.90}_{-1.41}$...
HFF6P-1247-6578	40.051970	-1.616066	0.82 ± 0.25	0.08 ± 0.17	27.60 ± 0.11	...	$2.05^{+1.75}_{-0.73}$...
HFF6P-1350-7372	40.056259	-1.627015	1.14 ± 0.36	0.22 ± 0.21	27.69 ± 0.12	...	$8.33^{+1.18}_{-6.56}$...
HFF6P-1194-8213	40.049783	-1.639252	> 1.83	-0.17 ± 0.19	27.81 ± 0.13	...	$8.89^{+0.97}_{-0.97}$...
HFF6P-1311-7372	40.054627	-1.627015	1.24 ± 0.30	-0.05 ± 0.24	28.02 ± 0.17	...	$8.49^{+0.93}_{-6.68}$...
HFF6P-1293-6262	40.053900	-1.607296	> 1.83	-0.19 ± 0.22	28.03 ± 0.16	...	$8.90^{+0.97}_{-6.47}$...
HFF6P-1514-7171	40.063097	-1.621433	1.46 ± 0.67	-0.15 ± 0.28	28.29 ± 0.20	...	$8.61^{+5.10}_{-7.00}$...

^a Total magnitudes m_{tot} estimated with the aperture correction $m_{\text{tot}} = m_{\text{AP}} - 0.82$.

^b Magnifications calculated with mass models in Kawamata et al. (2017).

^c References. (1)Atek et al. (2014), (2)Atek et al. (2015a), (3)Coe et al. (2015), (4)Laporte et al. (2014), (5)Laporte et al. (2015), (6)Laporte et al. (2016), (7)Livermore et al. (2017), (8)McLeod et al. (2016), (9)Oesch et al. (2015) (10)Zheng et al. (2014), (11)Zitrin et al. (2014)